Two-stage crustal growth in the Arabian-Nubian Shield: initial arc accretion followed by plume-induced crustal reworking

Hamed Gamal El Dien[1,2,*], Zheng-Xiang Li[1], Mohamed Abu Anbar[2], Luc-Serge Doucet[1], J. Brendan Murphy[1,3], Noreen. J. Evans[4], Xiao-Ping Xia[5], Jiangyu Li[1]

[1]Earth Dynamics Research Group, The Institute for Geoscience Research (TIGeR), School of Earth and Planetary Sciences, Curtin University, GPO Box U1987, Perth, WA 6845, Australia

[2]Geology Department, Faculty of Science, Tanta University, 31527 Tanta, Egypt

[3]Department of Earth Sciences, St. Francis Xavier University, Antigonish, Nova Scotia, Canada

[4]John de Laeter Centre, School of Earth and Planetary Sciences, Curtin University, GPO Box U1987, Perth, WA, 6845, Australia

[5]State Key Laboratory of Isotope Geochemistry, Guangzhou Institute of Geochemistry, Chinese Academy of Sciences, Guangzhou 510640, China

*Corresponding author: hamed.gamaleldien@curtin.edu.au

Abstract

Island-arc accretion during the assembly of Gondwana has been widely regarded as the main mechanism for Neoproterozoic crustal growth in the Arabian-Nubian Shield (ANS). However, processes involved to transform the newly accreted juvenile terranes into a typical continental crust remain unclear. Here, we present geochemical, isotopic, and U-Pb geochronological data from the El-Shadli volcanic province (80 km x 35 km and > 10 km thick) in the Eastern Desert of Egypt, which lies in the north-western part of the ANS and overlies strongly deformed, previously accreted arc terranes. The El-Shadli volcanic province consists mainly of a mafic–felsic bimodal suite and subordinate intermediate rocks that intrude the mafic rocks of the suite. The bimodal suite rocks are tholeiitic, whereas the intermediate rocks have a calc-alkaline affinity. The bimodal suite and the intermediate rocks both yield U-Pb zircon ages of ~700 Ma implying they are coeval. High zircon $\varepsilon Hf_{(t)}$ values for the bimodal suite (average $\varepsilon Hf_{(t)}$ = +11.46) as well as the intermediate rocks (average $\varepsilon Hf_{(t)}$ = +9.76) indicate they were either magmatic extractions derived directly from a depleted mantle source, or the products of remelting of juvenile crust. Oxygen isotope data for zircon yield similar $\delta^{18}O$ values for both the bimodal suite (average $\delta^{18}O$ = 4.94 ‰) and intermediate rocks (average $\delta^{18}O$ = 4.79 ‰). These are lower than typical mantle values and indicating the parental magma in both cases interacted with hydrothermal fluids. Based on the petrological, geochemical, and isotopic data, we suggest that the El-Shadli bimodal suite and the intermediate rocks were produced by reworking of MORB-like and arc-like oceanic lithosphere, respectively, most likely driven by a mantle plume during the break-up of Rodinia. The recognition of the El-Shadli volcanic province as a likely mantle plume-induced post-kinematic magmatism provides a mechanism for the transformation of newly accreted juvenile crustal terranes into a chemically stratified normal continental crust as we see today. In addition, such plume events may result in new mantle extractions that are converted into new continental crust.

Keywords: Neoproterozoic, crustal growth, crustal transformation, Arabian-Nubian Shield, mantle plume, rift magmatism

1. Introduction

There is a strong view that at least 60-70% of Earth's continental crust was mostly formed by the end of the Archean (2.5 Ga) (Arndt, 2013; Belousova et al., 2010; Dhuime et al., 2018, 2012; Hawkesworth et al., 2020; Taylor and McLennan, 1995). However, the mechanism(s) responsible for the generation of such continental crust and the processes related to crustal growth (including the geodynamic settings) are widely debated (Arndt and Davaille, 2013; Arndt, 2013; Hawkesworth et al., 2013, 2020; Kemp and Hawkesworth, 2014; Taylor and McLennan, 1995; Wang et al., 2020). In particular, few studies have considered how accreted juvenile crustal terranes were eventually transformed into the chemically stratified continental crust we see today.

Outcrops of Archean rocks are generally restricted to high-grade metamorphic terranes, and in most cases, deformation and metamorphism have substantially modified their original compositions and primary structures. These complications have led to the search for younger analogues of juvenile crustal generation/growth to investigate the mechanism(s) responsible for the crustal growth process. The Arabian-Nubian Shield (ANS) forms one of the largest exposures of Neoproterozoic juvenile continental crust on Earth (Fig. 1a: Pease and Johnson, 2013), and its crustal generation and cratonization/stabilization represent one of the largest events of continental crustal growth since the Archean (Bentor, 1985; Stern, 1994). The ANS crust is generally well exposed, and the low degrees of metamorphism make it one of the best areas to study continental crust formation.

Island-arc accretion during the assembly of Gondwana is generally considered to be the main mechanism for Neoproterozoic crustal growth in the ANS (Fritz et al., 2013; Johnson et al., 2011; Johnson and Woldehaimanot, 2003; Kröner et al., 1991; Stern, 1994, 2002). However, the size of the ANS and its Neoproterozoic growth rate significantly exceeds that of Cenozoic examples of crustal generation via the addition of juvenile mantle materials to arcs along subduction margins (Reymer and Schubert, 1986, 1984). Although mantle plume-related magmatism has been proposed as an alternative mechanism for Neoproterozoic crustal generation in the ANS (Stein, 2003; Stein and Goldstein, 1996), no direct record of Neoproterozoic plume events has been reported.

Bimodal volcanism produces intercalations of mafic and felsic rocks that are commonly found in magmatic rift systems above mantle plumes, such as the Cenozoic magmatism of the East-African rift (Rooney, 2020, 2017) and Neoproterozoic bimodal rift-related volcanism (Cheng et al., 2020; Kjøll et al., 2019; Li et al., 2010, 1999; X.-H. Li et al., 2008; Z. X. Li et al., 2003; Lyu et al., 2017). In their paleogeographic reconstruction of the Neoproterozoic supercontinent Rodinia, Z. X. Li et al. (2008) and Li et al. (2013) suggest that the ANS terranes were likely located between India, Australia-East Antarctica, and the Sahara craton, along the fringes of the Rodinia superplume at ~825–680 Ma. This time interval coincides with the rifting and fragmentation of the supercontinent Rodinia (Li et al., 2013; Z. X. Li et al., 2008; Li and Zhong, 2009), and is characterized by widespread plume-related bimodal volcanic and plutonic complexes, as well as mafic and ultramafic dikes, such as those reported in South China (Li et al., 1999; Z. X. Li et al., 2008, 2003; Wang et al., 2007), Tarim (Zhang et al., 2006), Australia (Wingate et al., 1998), Southern Africa (Frimmel et al., 2002) and Laurentia (Ernst et al., 2010; Ernst and Buchan, 2001; Heaman et al., 1992; Park et al., 1995).

Here, we describe a voluminous magmatic event in the El-Shadli volcanic province (80 km x 35 km and > 10 km thick) in the Eastern Desert of Egypt, which lies in the north-western part of the ANS (Figs. 1b and 2). Using whole-rock geochemical and Sr-Nd isotope data, and integrated U-Pb-Hf-O isotopic and trace element data from zircons, we investigate the origin and tectonic setting of this voluminous bimodal volcanism and examine the potential role of mantle plume-induced magmatism in the crustal growth of the Arabian-Nubian Shield.

2. Geological setting

2.1. Geological background

The East African Orogen (EAO) represents the largest orogen involved during the assembly of Gondwana, with orogenic activity peaking at ~650 Ma (Fritz et al., 2013; Merdith et al., 2017; Stern, 1994). The EAO consists of multiple zones of accretion and collision between East and West Gondwana, with the Neoproterozoic ANS located along its northern margin (Hamdy et al., 2017; Johnson et al., 2011; Johnson and Woldehaimanot, 2003; Pease and Johnson, 2013; Stern, 1994) (Fig. 1a). The ANS is divided into different terranes by several arc-arc suture zones marked by ophiolite belts (Fig. 1a; Johnson et al., 2011). The Eastern Desert of Egypt lies in the north-western part of the ANS (Fig. 1b). It is bounded to the south by the Onib-Sol Hamed-Gerf-Allaqi-Heiani suture zone (an ophiolitic belt; Fig. 1b), which is thought to have been obducted during arc accretion between ~800 and 720 Ma (Ali et al., 2010; Johnson et al., 2011). The crustal basement of the Eastern Desert (Fig. 1b) is predominantly composed of: (1) ~750–730 Ma dismembered ophiolites (Ali et al., 2010; Gamal El Dien et al., 2016, 2015; Kröner et al., 1992; Stern et al., 2004); (2) ~770–720 Ma arc-related metavolcanic and metasedimentary rocks (Abd El-Rahman et al., 2017; Ali et al., 2009; Bühler et al., 2014; Kröner et al., 1992; Stern and Hedge, 1985); (3) ~740–610 Ma granitoid rocks including diorites, tonalites, trondhjemites and granodiorites (Abdel-Rahman, 2018; El-Bialy et al., 2020; Eliwa et al., 2014; Moussa et al., 2008; Stern and Hedge, 1985; Gamal El Dien et al, under review); (4) ~730–630 gneisses, migmatites and metamorphic core complex (Ali et al., 2015, 2012a; Andresen et al., 2009; Augland et al., 2012; Kröner et al., 1994; Lundmark et al., 2012; Stern and Hedge, 1985); (5) ~700 Ma El-Shadli bimodal volcanic rocks (this study); (6) ~640–550 Ma alkaline A-type granites (Ali et al., 2013, 2012b; Eliwa et al., 2014; Lehmann et al., 2020; Moussa et al., 2008); (7) ~630–580 Ma post-collisional Dokhan (alkaline) volcanic rocks (Breitkreuz et al., 2010; Wilde and Youssef, 2000); and (8) ~610–585 Ma Hammamat molasse-type sedimentary rocks (Abd El-Rahman et al., 2019; Wilde and Youssed, 2002).

In this contribution, we focus on the volcanic rocks in the Eastern Desert of Egypt where Neoproterozoic metavolcanic-metasedimentary rock successions are widely distributed (Stern and Hedge, 1985) (Fig. 1b). These volcanic rocks were initially interpreted as the first stage of eugeosynclinal filling (Akaad and El-Ramly, 1960). Based on field observations and petrological and geochemical data, Akaad and El-Ramly (1960) classified the Eastern Desert volcanics into (1) an older metavolcanic series (the authors called "the El-Shadli type") and (2) a non-metamorphosed younger volcanic series (called the Dokhan type). Stern (1981) divided the Eastern Desert volcanic rocks into two groups: (1) Old Metavolcanics (OMV) and (2) Young Metavolcanics (YMV). The OMV group corresponds to ophiolite-related volcanic rocks and consists of low-K tholeiitic pillow metabasalts and basaltic andesites such as the El-Fawakhir ophiolites. The YMV group corresponds to arc-related volcanic (i.e. non-ophiolitic) rocks and comprises a low- to medium-K calc-alkaline suite including andesitic flows with subordinate mafic and felsic rocks, such as arc volcanics found in W. El-Dabbah and W. Arak. However, Stern (1981) did not recognise the presence of the non-metamorphosed El-Shadli bimodal volcanic province.

Khalil (1997), based on a comprehensive geochemical data compilation, suggested that the Eastern Desert volcanic rocks comprise ocean-related ophiolitic volcanics (i.e., OMV), intra-oceanic island arc-related volcanics (i.e., YMV), and the Dokhan volcanics (DV). The

DV mostly occurs in the northern part of the Eastern Desert (Fig. 1b) and is characterized by abundant felsic volcanic (rhyolite, dacite, and ignimbrite), with subordinate mafic and intermediate rocks. DV is un-metamorphosed, has a medium- to high-K calc-alkaline to alkaline affinity, and is interpreted to have been formed either in a continental arc (e.g., Khalil, 1997) or during a post-orogenic extension i.e., post-collision (Eliwa et al., 2006, 2014). Khalil (1997) classified the El-Shadli volcanic province (target of this work) as part of the YMV group.

More recent geochronological data demonstrate that the OMV (~750–730 Ma; Ali et al., 2010; Kröner et al., 1992; Stern et al., 2004), and the YMV (~770–720 Ma, e.g., Abd El-Rahman et al., 2017; Ali et al., 2009; Bühler et al., 2014; Kröner et al., 1992; Stern and Hedge, 1985) overlap in their ages. In contrast, the DV series has a distinctly younger age range (~630–580 Ma; Breitkreuz et al., 2010; Wilde and Youssef, 2000) (Fig. 1b).

The fit of the El-Shadli bimodal volcanic province in the OMV and YMV grouping of Stern (1981) has been debated for many years (e.g., Ali et al., 2009). Some consider the El-Shadli bimodal volcanic province to be genetically and temporally related to the OMV group (Akaad and El-Ramly, 1960; Akaad and Noweir, 1969; El-Shazly and El-Sayed, 2000), whereas others classify it as a member of the YMV (El-Gaby and El-Nady, 1984; Faisal et al., 2020; Khalil, 1997). Alternatively, Stern et al. (1991) suggested that the El-Shadli bimodal volcanics formed in a magmatic rift setting, implying they are unrelated to either metavolcanic group. The age of the El-Shadli bimodal volcanics, determined by a Rb-Sr whole-rock isochron from mafic and felsic rocks around the Um Samiuki area (Black box in Fig. 2), was reported as 712 ± 24 Ma (Stern et al., 1991), i.e. younger than the previously reported ages of both the OMV and YMV. The most recent LA-ICPMS U-Pb zircon data from felsic rocks around the Abu Hamamid area (Black box in Fig. 2) yield an age of 695 ± 6 Ma (Faisal et al., 2020).

2.2. Field relationships, observations and petrography

The El-Shadli area is located in the southern part of the Eastern Desert (Figs. 1b and 2). Neoproterozoic rocks exposed in this area include the El-Shadli bimodal volcanic rocks, the El-Shadli granitoids-gabbro association, the W. Ghadir ophiolitic assemblages, the W. Hafafit core complex, post-collisional alkaline granites, and post-collisional W. Ranga volcanics (Fig. 2). The El-Shadli volcanic province is the largest bimodal volcanic suite in the Eastern Desert of Egypt (80 km x 35 km and > 10 km thick) (Khudeir et al., 1988; Shukri and Mansour, 1980; Stern et al., 1991). This province trends approximately E-W, and is surrounded by outcrops of the El-Shadli granitoids-gabbro association (~730–720 Ma: Gamal El Dien et al., under review) (Fig. 2). The El-Shadli volcanic province consists of massive, dominantly submarine bimodal volcanic lavas and tuffs, with interbedded immature metasedimentary rocks and subordinate intermediate volcanic rocks (Figs. 3 and 4). The rocks in this province were folded into a WNW-ESE symmetric syncline flanked by two regional-scale anticlines and are cut by several WNW-ESE-trending normal and thrust faults that are oriented parallel to the main folds and are characterized by locally intense shearing (Khudeir et al., 1988; Shukri and Mansour, 1980; Stern et al., 1991) (Fig. 2).

Stratigraphically, an unconformable contact separates the El-Shadli bimodal volcanic province from the underlying and surrounding El-Shadli granitoids (729 ± 7 Ma: Gamal El Dien et al., under review). In addition, mafic dyke swarms intrude the granitoids with regular and sharp contacts (Fig. 4a-e). These mafic dykes have the same geochemical composition of the mafic rocks of the bimodal volcanic suite (see geochemistry section), and we interpret them to be possible feeder dykes for the mafic rocks of the bimodal volcanic suite (sample S01-2, Fig. 4a). These dykes are up to 1 m in width and have well-developed chilled margins (Fig. 4be). The granitoids and mafic dykes are both intruded by thin felsic dykes (sample S01-3) (Fig. 4a). These observed field relationships, along with new isotopic ages (see below), argue against models suggesting that the El-Shadli granitoids-gabbro association intruded the volcanic province (Abdel-Karim et al., 2019; Faisal et al., 2020; Khudeir et al., 1988; Shukri and Mansour, 1980; Stern et al., 1991) and instead suggest that the El-Shadli bimodal volcanics are younger than the surrounding El-Shadli granitoids-gabbro association. These previous models focused on an outcrop around the Um Samiuki-Abu Hamamid area (yellow stars in Fig. 2), which is not in direct contact with the surrounding granitoids-gabbro association. Our geochronological data show that the El-Shadli bimodal volcanics (698 ± 6 Ma; see result section below) are 30–20 Ma younger than the El-Shadli granitoids-gabbro association. Structurally, the both El-Shadli bimodal volcanics and granitoids-gabbro association show the same structural trends, and were affect by WNW-ESE-trending normal faults and shearing (see a review of Fowler and Hamimi, 2021) (Fig. 2).

Regionally, the El-Shadli granitoids-gabbro association that underlies the El-Shadli bimodal volcanics intrudes the strongly deformed and variably metamorphosed ca. 750 Ma Wadi Ghadir ophiolite assemblages (Abdel El-Wahed et al., 2019; Youssef et al., 2000) (Fig. 2), indicating that both the volcanics and the plotonic intrusions formed after regional-scale terrane accretion.

The bimodal volcanic rocks consist of massive alternating mafic and felsic layers that range from a few to hundreds of meters in thickness, and include some sills (Fig. 3). The mafic rocks mainly consist of submarine tholeiitic basalts, basaltic andesites, and few dolerite sills (sample S04-2) with thin intercalations of tuffs and cherts (Fig. 4f). These mafic rocks are generally massive and, in some localities, show pillow structures ranging from a few centimetres to meters in width with vesicular margins (Figs. 3 and 4g). The felsic rocks mainly consist of massive rhyolitic lava flows (Fig. 3). The volcanogenic sedimentary rocks are mainly laminated tuffs and agglomerates (Fig. 4k, f). Subordinate intermediate rocks occur as small un-mappable bodies that intrude the mafic rocks (Fig. 4h-j).

Petrographically, the El-Shadli bimodal volcanics are remarkably fresh with preservation of original minerals and textures, although locally some greenschist facies mineral assemblages are present (Fig. 5). The mafic rocks are composed of plagioclase, and clinopyroxene and display intergranular to porphyritic textures (Fig. 5a-f). Plagioclase occurs as phenocrysts, small laths, and in the fine-grained groundmass (Fig. 5a-c). These phenocrysts are commonly euhedral with albite twinning and show secondary alteration to epidote. Clinopyroxene exists as micro-phenocrysts (up to 1 mm in length) in ophitic and sub-ophitic intergrowths with plagioclase laths (Fig. 5e). Clinopyroxene may be altered to amphibole and chlorite (Fig. 5f). Amphiboles are mainly pale green actinolites and occur in the groundmass (Fig. 5f). Opaque minerals include magnetite, hematite, and ilmenite, and occur as fine subhedral grains randomly distributed in the groundmass (Fig. 5f). Other accessory minerals include titanite and apatite. Epidote, sericite, clay minerals, chlorite, and calcite occur as secondary minerals.

The felsic rocks are mainly massive reddish to pink-grey rhyolites (Fig. 3) and are typically composed of plagioclase, quartz, potash feldspar (orthoclase), and minor biotite (Fig. 5g-j). Opaque minerals include magnetite; titanite and zircon occur as accessory minerals. Secondary minerals include chlorite, epidote, sericite, and clay minerals. Plagioclase, quartz, and potash feldspar occur either as euhedral to subhedral phenocrysts and/or small grains in the groundmass (Fig. 5g-i). Plagioclase crystals have well persevered albite twinning, and display slight epidote alteration (Fig. 5g). Some quartz grains exhibit wavy extinction (Fig. 5h). Potash feldspar phenocrysts show Carlsbad twinning (Fig. 5i). Biotite occurs in the groundmass and shows chlorite alteration along cleavage (Fig. 5j).

The intermediate volcanics include grey, porphyritic andesitic rocks (Fig. 4h-j) consisting of plagioclase, quartz, and mafic minerals (hornblende and biotite) (Fig. 5k, l). Opaque minerals include magnetite, ilmenite, and titanite, and zircon occurs as accessory minerals. Secondary minerals include chlorite, epidote, and sericite. Plagioclase, quartz, and biotite occur as large phenocrysts in the groundmass of the same minerals (Fig. 5k). Hornblende occurs as small grains within the groundmass. Chlorite represents an alteration product from biotite (Fig. 5l). Epidote and sericite are disseminated in the groundmass as alteration products of plagioclase (Fig. 5k).

3. Analytical methods

Analytical techniques are described in detail in the supplementary information (Tables S1 to S3). Whole-rock major elements were determined for 18 samples (11 mafic, 5 felsic, and 2 intermediate rock samples) using X-ray fluorescence at the Bureau Veritas Lab, Perth (Supplementary Table S1). Whole-rock trace elements and Sr-Nd isotope data were determined using inductively coupled plasma mass spectrometry (ICP-MS) and thermal ionization mass spectrometry (TIMS), respectively, at the Macquarie (MQ) GeoAnalytical Lab, Macquarie University (Supplementary Table S1). Zircon U-Pb dating was carried out using SHRIMP II at Curtin University (Supplementary Table S2) for rhyolite sample S02-5 and andesite sample S16. Zircon Hf isotope and trace element data were acquired using laser ablation split stream ICP-MS (LA-SS-ICP-MS) in the John de Laeter Centre, Curtin University (Table S3); zircon O isotope data were acquired using secondary ion mass spectrometry (SIMS) at the Guangzhou Institute of Geochemistry, China (Table S3).

4. Results

4.1. Whole-rock geochemical data

Samples of the El-Shadli volcanic rocks are fresh with minor alteration/weathering, as indicated by low loss on ignition (LOI) with values below 1 wt. % for felsic rocks and ranging between 1 to 3 wt. % for the mafic and intermediate rocks (Supplementary Table S1). As rock composition can be modified by alteration/weathering (Polat and Hofmann, 2003), the effect of alteration on the mobility of the major and trace elements was evaluated before discussing the geochemical and petrological characterizations of the studied volcanic rocks. The LOI value was plotted against all major and some trace elements such as Cr, Ni, Rb, Sr, Y, Zr, Nb, Ba, La, and Ce (Supplementary Figs. S1 and S2). None of the major and trace elements shows any correlation with the LOI values, suggesting that there is no significant effect of alteration/weathering on the geochemical composition of the studied rocks.

The El-Shadli volcanic rocks have a wide range of SiO_2 contents (45.5–77.2 wt. %) and show a clear bimodal distribution (Supplementary Fig. S3). On a total alkali versus silica (TAS: Middlemost, 1994) plot (Fig. 6a), two major subgroups are defined (including data from this study and that of previous work (Abdel-Karim et al., 2019; Faisal et al., 2020; Khudeir et al., 1988; Shukri and Mansour, 1980; Stern et al., 1991). The first subgroup comprises basalt with a minor amount of basaltic andesite, and the other subgroup consists of rhyolite along with a subordinate number of intermediate rocks. The intermediate rocks include only andesite samples from this study (S16 and S17-1) and three samples from Stern et al. (1991) and Faisal et al. (2020). The geochemical distinction between the two subgroups is evident the plot of Zr/Ti versus Nb/Y (Fig. 6b; Winchester and Floyd, 1976).

Data from this study show that the mafic (i.e., basaltic) rocks have SiO_2 (45.5–51.5 wt. %), MgO (4.2–9.2 wt. %), Al_2O_3 (14.6–18.1 wt. %), $Fe_2O_3^T$ (8.6–13.7 wt. %), and TiO_2 (0.6–1.3 wt. %) (Supplementary Fig. S3 and Table S1). The felsic rocks have SiO_2 (74.1–77.2 wt. %), MgO (0.1–0.6 wt. %), Al_2O_3 (11.3–13.2 wt. %), $Fe_2O_3^T$ (1.6–3.5 wt. %), and TiO_2 (0.1–

0.3 wt. %) (Supplementary Fig. S3 and Table S1). The two intermediate rocks (S16 and S17-1) have compositions of SiO_2 = 69.1 and 58.1 wt. %, MgO = 1.1 and 1.9 wt. %, Al_2O_3 = 15.7 and 18.6 wt. %, $Fe_2O_3^T$ = 3.4 and 6.3 wt. %, and TiO_2 = 0.3 and 0.9 wt. %, respectively (Supplementary Fig. S3 and Table S1). Overall, the mafic and felsic rocks studied herein have a very low K_2O content (<1 wt. %), but the intermediate rocks have >1 wt. % K_2O (Fig. 6d). For the basaltic samples, the total alkalis ($Na_2O + K_2O$ = 1.7–4.8 wt. %) increase with increasing SiO_2 (Supplementary Fig. S3 and Fig. 6a). In contrast, the total alkalis ($Na_2O + K_2O$ = 3.6–6.2 wt. %) decrease with increasing SiO_2 in the felsic rocks, (Supplementary Fig. S3 and Fig. 6a). The intermediate rocks show no systematic relationship between total alkalis ($Na_2O + K_2O$ = 5.7 wt. %) and SiO_2 (Supplementary Fig. S3 and Fig. 6a).

All of the studied rocks have a sub-alkaline affinity according to their low total alkalis (Middlemost, 1994) and low Nb/Y ratios (Winchester and Floyd, 1976) (Fig. 6a, b). On an AFM diagram, they display a tholeiitic series trend (Fig. 6c). The SiO_2 versus K_2O relationship (Peccerillo and Taylor, 1976) shows that the basaltic and felsic rocks belong to the tholeiitic series (Fig. 6d), while the intermediate rocks are more akin to calc-alkaline series rocks. These interpretations are supported by petrogenetically-sensitive trace element ratios. According to Co-Th (Hastie et al., 2007) and Th/Yb versus Zr/Y (Ross and Bédard, 2009) diagrams, both the basaltic and felsic rocks are similar to the tholeiitic series, whereas the intermediate rocks show a calc-alkaline affinity (Figs. 6e, f).

On the chondrite (CI)-normalized (Anders and Grevesse, 1989) rare earth element (REE) diagram (Fig. 7a, b), the basaltic and felsic rocks commonly show relatively flat REE patterns with a slightly negative slope for the light REE (LREE), similar to MORB (Sun and McDonough, 1989). The basaltic rocks show slight LREE-depletion with La_N = 3.04–7.23, $(La/Sm)_{CI}$ = 0.42–0.75, $(La/Yb)_{CI}$ = 0.46–0.95, relatively flat heavy REE patterns (HREE; $(Yb/Gd)_{CI}$ = 0.82–1.35) and an insignificant negative Eu anomaly [$(Eu/Eu^*)_{CI}$ = 0.90–1.1, where Eu* = √(Sm × Gd)] (Fig. 7a). The felsic rocks have more evolved (higher) REE compositions, but mimic the REE patterns of the basaltic rocks, with La_N = 11.54–24.93, $(La/Sm)_{CI}$ = 0.63–1.12, $(La/Yb)_{CI}$ = 0.64–1.07 and $(Yb/Gd)_{CI}$ = 0.92–1.27, with the exception of pronounced negative Eu anomalies [$(Eu/Eu^*)_{CI}$ = 0.55–0.85] (Fig. 7b). The intermediate rocks display REE patterns that are distinct from both the basaltic and felsic rocks (Fig. 7c), with a positive trend from LREE to HREE with LREE-enrichment La_N = 22.05–22.14, $(La/Sm)_{CI}$ = 1.46–1.91, and $(La/Yb)_{CI}$ = 2.89–5.49.

On the normal-MORB (NMORB)-normalized trace elements diagram (Sun and McDonough, 1989) (Fig. 7a), the basaltic rocks display depletion in Zr and Nb, but are relatively enriched in large ion lithophile elements (LILE) such as Cs, Rb, Ba, Th, and U. The felsic rocks exhibit strongly fractionated patterns relatively to N-MORB with significant negative Nb, P, and Ti anomalies (Fig. 7b). The intermediate rocks, however, show significant enrichments in almost all trace elements compared to N-MORB (Fig. 7c).

4.2. Whole-rock Sr-Nd isotopic data

The basaltic rocks have low Sr (149–209 ppm) and Rb (0.49–18.06 ppm) contents. Their measured $^{87}Sr/^{86}Sr$ ratios range from 0.702503 ± 0.000005 to 0.705022 ± 0.000003 (Fig. 8a and Supplementary Table S1) with calculated initial $^{87}Sr/^{86}Sr$ from 0.702219 ± 0.000003 to 0.702694 ± 0.000003. They also have low Nd (4–16 ppm) and Sm (1.5–5.6 ppm) abundances, and measured $^{143}Nd/^{144}Nd$ ratios ranging from 0.512950 ± 0.000004 to 0.513135 ± 0.000002 (Fig. 8a and Supplementary Table S1). Calculated initial $^{143}Nd/^{144}Nd$ values range from 0.512030 ± 0.000005 to 0.512105 ± 0.000002 (Fig. 8b and Supplementary Table S1) which correspond with εNd(t) values (t = 700 Ma) ranging from +5.84 to +7.31 (Fig. 8b).

The felsic rocks have similar Sr and Nd isotopic composition to the basaltic rocks with initial ratios of $^{87}Sr/^{86}Sr$ = 0.702575 ± 0.000004 – 0.703043 ± 0.000003, $^{143}Nd/^{144}Nd$ =

0.512065 ± 0.000002 – 0.512115 ± 0.000002, and εNd(t) values ranging from +6.53 to +7.50 (Fig. 8b and Supplementary Table S1). The intermediate rocks display significantly different isotopic compositions, with initial ratios of $^{87}Sr/^{86}Sr$ in the range of 0.702527 ± 0.000004 – 0.702605 ± 0.000003, $^{143}Nd/^{144}Nd$ 0.511677 ± 0.000001 – 0.511802 ± 0.000006, and εNd(t) between +1.38 and –1.04 (Fig. 8b and Supplementary Table S1).

4.3. Zircon U-Pb-Hf-O isotopes and trace elements

4.3.1. Rhyolite sample S02-5

Zircon grains from sample S02-5 are typically < 100 μm in length and display a euhedral equant to prismatic morphology. In cathodoluminescence (CL) images, these zircons display well-developed oscillatory zoning, although some have unzoned homogenous cores (Fig. 9a) and patchy zoning (Fig. 9a).

Twenty-seven U-Pb SHRIMP analyses were conducted on 27 grains. These analyses have variable U (22–112 ppm) and Th (6–65 ppm) contents, as well as Th/U ratios (0.23–0.58) (Supplementary Table S2) indicating a magmatic origin and crystallization from high SiO_2 magma (Kirkland et al., 2015). On the Tera-Wasserburg diagram, the 27 analyses yield a weighted mean $^{206}Pb/^{238}U$ age of 698 ± 11 Ma (±95 % conf., MSWD = 1.19, N = 27; Fig. 9a), interpreted to represent the crystallization age of the rhyolite sample S02-5.

Fifty-three laser ablation split stream (LASS) analyses were conducted on 53 zircon grains from the same sample. Twenty-seven analyses were placed over the SHRIMP spots. The LASS analyses yield a weighted mean $^{206}Pb/^{238}U$ age of 698 ± 6 Ma (±95 % conf., MSWD = 0.53, N = 46; Fig. 9b and Supplementary Table S3), which is almost identical to the SHRIMP age. CI-normalized (Anders and Grevesse, 1989) zircon REE patterns show a negative slope from middle to heavy REE [$(Yb/Gd)_{CI}$ =12–32], negative Eu anomalies [$(Eu/Eu^*)_{CI}$ = 0.12–

0.41], and variable Ce anomalies [$(Ce/Ce^*)_{CI}$ = 0.36–20, where Ce* = √(La × Pr)] that are characteristic of unaltered magmatic zircon (Belousova et al., 2002; Grimes et al., 2015) (Fig. 10a and Supplementary Table S3). Zircon grains have Hf contents of 7975–8767 ppm, Nb contents of 0.56–6.16 ppm, U/Yb ratios of 0.04–0.11 (Fig. 10b-d and Supplementary Table S3).

The Lu-Hf isotopic data from these 53 spots yield $^{176}Lu/^{177}Hf$ ratios of 0.00191 ± 0.00001 – 0.00941 ± 0.00010 and $^{176}Hf/^{177}Hf_{(t)}$ ratios of 0.282517 ± 0.000028 – 0.282756 ± 0.000062 (Supplementary Table S3). The calculated $\varepsilon Hf_{(t)}$ values range from +7.38 ± 0.42 to +15.14 ± 0.93 and yield an average value of +11.46 (Fig. 11 and Supplementary Table S3) that corresponds to T_{DM} Crustal ages of 0.70–1.19 Ga. Twenty-seven SIMS O isotope spots have $\delta^{18}O$ values within the range of 4.50 ± 0.18 ‰– 5.24 ± 0.18 ‰ with an average value of 4.94 ‰ (Fig. 11b and Supplementary Table S3).

4.3.2. Andesitic sample S16

Zircon grains from sample S16 are prismatic with euhedral rims and range in length from 100–200 μm. These zircons have homogenous textures and well-developed oscillatory zoning in CL images (Fig. 9c). Some grains show only faint and broad zoning (Fig. 9c).

Twenty U-Pb SHRIMP analyses were conducted on 20 grains. The analysed grains have variable U (33–300 ppm), Th (19–150 ppm), and Th/U ratios (0.26-0.58) (Supplementary Table S2) that signify a magmatic origin (Kirkland et al., 2015). On the Tera-Wasserburg diagram, 19 of the 20 analyses yield a weighted mean $^{206}Pb/^{238}U$ age of 698 ± 8 Ma (±95 % conf., MSWD = 1.6, N = 19; Fig. 9c), interpreted as the crystallization age of this andesitic sample.

Forty-three LASS analyses were conducted on 43 grains from the same sample with 26 analyses performed over the SHRIMP spots. Forty-two LASS analyses yield a weighted mean $^{206}Pb/^{238}U$ age of 707 ± 5 Ma (±95 % conf., MSWD = 1.16, N = 42; Fig. 9d and Supplementary Table S3) which is consistent (within error) with the SHRIMP age. One grain, S16@4, has an older $^{206}Pb/^{238}U$ age of 854 ± 25 Ma (± 2σ) and may represent a xenocryst from an older Neoproterozoic ANS rock such as the 845 ± 5 Ma arc-related granitoids from the Asir terrane, Saudi Arabia (Robinson et al., 2014) (Fig. 9d and Supplementary Table S3). CI-normalized (Anders and Grevesse, 1989) zircon REE patterns show a negative slope from the middle to heavy REE [$(Yb/Gd)_{CI}$ = 2.3–46] and high negative Eu anomalies [$(Eu/Eu^*)_{CI}$ = 0.17–0.71] which are characteristic of unaltered magmatic zircons (Belousova et al., 2002; Grimes et al., 2015) (Fig. 10a and Supplementary Table S3). The zircon grains have Hf contents of 8768–12530 ppm, Nb contents of 0.27–2.14 ppm, and U/Yb ratios of 0.05–0.65 (Fig. 10b-d and Supplementary Table S3).

The Lu-Hf isotopes of these 42 spots yield $^{176}Lu/^{177}Hf$ ratios of 0.00041 ± 0.00004 – 0.00198 ± 0.00001 and $^{176}Hf/^{177}Hf_{(t)}$ ratios of 0.282556 ± 0.000038 – 0.282686 ± 0.000047 (Supplementary Table S3). The calculated $\varepsilon Hf_{(t)}$ values range from +7.38 ± 0.57 to +11.96 ± 0.81 and give an average of +9.76 (Fig. 11), corresponding to T_{DM} crustal ages of 0.85–1.14 Ga. Grain S16@4 has $^{176}Lu/^{177}Hf$ ratios of 0.000024 ± 0.00001, $^{176}Hf/^{177}Hf_{(t)}$ ratio of 0.282625 ± 0.000061 and $\varepsilon Hf_{(t)}$ value of +13.43 ± 0.92 corresponding to a T_{DM} crustal age of 0.88 Ga. A total of 20 SIMS O isotopic analyses yield $\delta^{18}O$ values ranging from 4.27 ± 0.16 ‰ to 5.23 ± 0.16 ‰ with an average of 4.79 ‰ (Fig. 11b and Supplementary Table S3).

5. Discussion

5.1. Tectonic setting of the El-Shadli bimodal volcanic province

The tectonic affinity of the El-Shadli bimodal volcanic province is controversial, with some arguing that the province was formed in an island arc setting (Abdel-Karim et al., 2019; Faisal et al., 2020; Khudeir et al., 1988; Shukri and Mansour, 1980) and others suggesting a continental rift-related origin (Stern et al., 1991). The latter interpretation was supported by relatively few geochemical data from a small sampling area at W. Abu-Hamamid (yellow star in Fig. 2), within the El-Shadli bimodal volcanic province. The following section presents a detailed discussion with new evidence in support of a rift-related origin.

Field observations show clear intercalation between mafic and felsic rocks (Fig. 3) which is characteristic of magmatic rift systems, i.e. the Cenozoic magmatism in the East-African rift (Rooney, 2020, 2017) and known Neoproterozoic bimodal rift volcanics in South China and Tarim (Cheng et al., 2020; Kjøll et al., 2019; Li et al., 2010, 1999; X.-H. Li et al., 2008; Z. X. Li et al., 2003; Lyu et al., 2017). In addition, there is no field evidence within the El-Shadli volcanic province of either upper mantle rocks such as peridotites and serpentinites, and/or sheeted dykes, which argues against these rocks being part of an ophiolite assemblage (see Furnes et al., 2014). In contrast, well-defined ophiolite sections are exposed both to the south (~750 Ma MORB-related Gerf ophiolites; Zimmer et al., 1995) and north (~750-730 Ma arc-related El-Fawakhir and W. Ghadir ophiolites; Abd El-Rahman et al., 2009b, 2009a; Basta et al., 2011; El-Sayed et al., 1999) of the study area. The deformation style and structural trends of the El-Shadli bimodal volcanic province and the surrounding El-Shadli granitoid complex are also in sharp contrast with those of accreted ophiolite assemblages (Fig. 2) with the latter featuring much stronger deformation and varying degree of metamorphism (up to amphibolite facies; Abdel El-Wahed et al., 2019; Fowler and Hamimi, 2021; Youssef et al., 2000).

The bimodal chemical composition is atypical of either modern oceanic (e.g. Izu-Bonin-Marian, IBM) or continental (e.g. Andean) arcs but is common in continental rifts (e.g. East-African) (Fig. 12a-e). We compare the SiO_2 content of the El-Shadli volcanic province (data from both this study and previous work: Faisal et al., 2020; Khudeir et al., 1988; Shukri and Mansour, 1980; Stern et al., 1991) with other Eastern Desert volcanic rocks such as (1) ophiolite-related volcanics (Abd El-Rahman et al., 2009b, 2009a; Basta et al., 2011; El-Sayed et al., 1999; Stern, 1981), (2) arc-related volcanics (Ali et al., 2009), and (3) the post-collisional Dokhan volcanics (Eliwa et al., 2006, 2014) (Fig. 12a-d). The El-Shadli volcanics display a distinct bimodal magmatic nature similar to that of the East-African rift-related volcanics, which is different from that of typical ophiolite- or arc-related volcanics. It is also atypical of any other Neoproterozoic volcanic assemblages in the Eastern Desert (Fig. 12b-e).

In Harker variation diagrams (Supplementary Fig. S4), arc-related volcanics typically display a linear correlation with SiO_2. The East-African rift-related volcanics, on the other hand, show a continuous, non-linear (i.e., hyperbolic) trend with more dispersion (Martin and Piwinskii, 1972; Peccerillo et al., 2003) (Supplementary Fig. S4), which is similar to that observed in the El-Shadli volcanics. These trends are particularly evident in the Al_2O_3, Na_2O, and K_2O contents of the mafic and felsic El-Shadli volcanics, and in almost all major oxides from the mafic rocks (Supplementary Fig. S3 and Fig. 6). Thus, we conclude that the El-Shadli bimodal volcanics display similar major elemental relationships with SiO_2 content (Supplementary Fig. S3) as that documented for well-known rift-related volcanics (Supplementary Fig. S4).

Whole-rock REE and Nd-Sr isotopic data together with zircon trace element data for the El-Shadli mafic and felsic rocks show a typical MORB-like composition and are atypical of arc-related basalts and granites, respectively (Figs. 7a, b, 8, and 10). On the other hand, the whole-rock geochemical, isotopic, and zircon trace element data of the intermediate rocks have an arc-like signature, the origin of which is discussed below.

On discrimination plots of immobile trace element data (Figure 13a-c) such as the V vs Ti (Shervais, 1982; X.-C. Wang et al., 2016), Sm-Ti-V (Vermeesch, 2006), and TiO_2/Yb versus

Nb/Yb (Pearce, 2008) diagrams, the El-Shadli mafic rocks plot in the MORB field and are similar to Basin and Range rift-related basalts (X.-C. Wang et al., 2016), suggesting that the El-Shadli mafic rocks were emplaced in a rift environment. Similarly, on geochemical classification diagrams for the felsic rocks, such as the Ga/Al vs FeO_T/MgO (Whalen et al., 1987) and SiO_2 versus $FeO_T/(FeO_T + MgO)$ (Fig. 13d; Frost et al., 2001), the El-Shadli samples are typical of A-type granites which generally form in within plate/rift-related environments (Bonin, 2007; Whalen et al., 1987). On the Rb vs. (Y + Nb) and Nb vs. Y diagrams (Fig. 13e, f) that link the magmatic source with the tectonic setting of the felsic rocks (Pearce, 1996; Pearce et al., 1984; Whalen and Hildebrand, 2019), the El-Shadli felsic rocks plot close to ocean ridge granites (ORG) and slightly overlap with within-plate granites (WPG), supporting a rift-related origin.

In summary, based on field observations and geochemical data, the El-Shadli bimodal volcanics most likely formed in a rift-related tectonic setting (Stern et al., 1991).

5.2. Source region and petrogenesis of the El-Shadli bimodal suite

5.2.1. Nature of the parental magma and magma source

In order to evaluate if the El-Shadli bimodal volcanics originated from the melting of crust or from a mantle source, evidence for crustal contamination in the parent melts needs to be assessed. The low abundance (<10 ppm) of Rb (a fluid-mobile element: FME) in the El-Shadli felsic rocks (and even mafic rocks) indicates an inherited depleted mantle source and the absence of interaction/contamination with the continental crust (Pearce, 1996; Pearce et al., 1984) (Fig. 13e, f). Also, the low initial $^{87}Sr/^{86}Sr$ ratios (0.702219–0.703043) and highly positive εNd(t) (from +5.84 to +7.50) of the El-Shadli mafic and felsic rocks (Fig. 8b) indicate the juvenile nature of the parental magma, with no detectable crustal contribution to their compositions. This parental magma was likely extracted from a depleted MOR-like source

(Figs. 7a, b, 8, and 10). The El-Shadli bimodal suite has a tholeiitic affinity with a parental magma characterized by a very low K_2O content (Fig. 6).

Zircon U-Pb analyses of rhyolite sample S02-5 indicate a lack of pre-Neoproterozoic inherited cores or zircon xenocrysts (Fig. 9a), implying no detectable interaction with old crustal materials (Belousova et al., 2015; Carley et al., 2014; Grimes et al., 2015), consistent with a juvenile parental magma composition (i.e. a depleted source). Variations of U/Yb ratio in zircon reflect variations in the melt composition at the time of zircon crystallization (Grimes et al., 2007). The U/Yb ratio for the bulk continental crust is 0.7 (Rudnick and Gao, 2014) compared to 0.02 for MORB (White and Klein, 2014). The low U/Yb ratios (typically < 0.1) of the analyzed zircons from rhyolite sample S02-5 are similar to zircons formed from a depleted MOR source and are significantly lower than continental and arc-related zircons (Carley et al., 2014; Grimes et al., 2015, 2007) (Fig. 10). The low Nb/Yb and Gd/Yb ratios of these zircons are also typical of zircons extracted from a depleted MOR source (Grimes et al., 2015) (Fig. 10).

Hf isotopic compositions of zircons provide significant constraints on the nature and compositional evolution of the parental magma and are sensitive to the relative contributions from the continental crust and depleted mantle of different ages (Belousova et al., 2010; Griffin et al., 2002; Kemp and Hawkesworth, 2014; Vervoort and Blichert-Toft, 1999). As Hf is more incompatible than Lu during mantle partial melting processes, it is highly enriched in the continental crust, leading to a depleted mantle source that becomes more radiogenic (i.e. high Lu/Hf and higher $^{176}Hf/^{177}Hf$) with time. The continental crust becomes less radiogenic with time (low Lu/Hf and lower $^{176}Hf/^{177}Hf$) (Kinny et al., 1991; Patchett, 1983; Patchett et al., 1981). As Hf strongly partitions into zircon, the Hf concentration in zircon is high (0.5–2 %) and the Lu/Hf ratio is very low (<0.001) (Kemp and Hawkesworth, 2014; Patchett, 1983). Therefore, zircon preserves the near initial $^{176}Hf/^{177}Hf$ ratio of the source magma at the time of crystallization (Hawkesworth and Kemp, 2006; Vervoort and Blichert-Toft, 1999) and can fingerprint both the magma source, as well as the potential presence of older continental crust and depleted mantle of different ages (Belousova et al., 2010; Griffin et al., 2002; Kemp et al., 2006; Kemp and Hawkesworth, 2014; Kinny et al., 1991; Kinny and Maas, 2003; Vervoort and Blichert-Toft, 1999). The highly positive zircon $\varepsilon Hf_{(t)}$ values (from +7.38 ± 0.42 to +15.14 ± 0.93) of rhyolite sample S02-5 (Fig. 11) indicate the parental magma was extracted from a juvenile source with no detectable involvement of old continental crust (Belousova et al., 2010; Hawkesworth and Kemp, 2006).

O isotopes in zircon are sensitive to parental magma contamination by continental and sedimentary materials (Valley, 2003). The $\delta^{18}O$ values of typical mantle-like magma (5.3 ± 0.3‰) are shifted to lower values by interaction with hydrothermal fluids or to higher values by interaction with a source that underwent sediment and/or crustal recycling (Hawkesworth and Kemp, 2006; Valley, 2003; Valley et al., 2005, 1998). The low $\delta^{18}O$ values (4.50 ± 0.18 – 5.24 ± 0.18 ‰) of the zircons in rhyolite sample S02-5 indicate that their parental magma interacted with high-temperature hydrothermal fluids (Grimes et al., 2013; H. Wang et al., 2016) (Fig. 11).

Taken together, the whole-rock geochemical and isotopic compositions of the El-Shadli mafic and felsic rocks are consistent with derivation from a depleted MOR-like source rather than from an arc-related source. The zircon O isotopic data, together with the enrichment of the El-Shadli mafic and felsic rocks in some LILE (e.g. Cs, Ba, and U) relative to N-MORB (Fig. 7), is likely related to hydrothermal alterations of the MOR-like source (Koepke et al., 2005; Tao et al., 2020). Finally, the whole-rock Nd-Sr isotopic and geochemical data, along with the zircon U-Pb-Hf-O-trace element data, suggest that the parental magma was juvenile and was not affected by continental crustal contamination. Thus, we suggest that the parental magmas of the El-Shadli bimodal volcanics were extracted from a depleted MOR-like source that had undergone hydrothermal alteration due to fluid circulation in an oceanic setting.

5.2.2. Petrogenesis

The El-Shadli mafic rocks have an evolved composition with low Mg# [MgO/ (MgO + FeO^T)*100] = 64–43, Cr (9–341 ppm), and Ni (3–120 ppm) (Supplementary Table S1). These Mg #, Cr, and Ni contents are significantly lower than those of primary mantle melts (Ni > 500 ppm, Cr > 1000 ppm, and Mg# > 72: Niu and O'Hara, 2008), suggesting these volcanics are not primary mantle melts but have evolved by fractionation (Cheng et al., 2020; Li et al., 2002). In Harker plots (Supplementary Fig. S3), the mafic rocks show a decrease in MgO, $Fe_2O_3^{T,}$ and CaO with increasing $SiO_{2,}$ which, together with the wide range in Ni and Cr, indicate significant fractional crystallization of olivine and clinopyroxene. Thus, this mafic magma was a product of high degree partial melting of a depleted source (a two-stage formation process after primary partial melting of mantle peridotites). Such a source is most likely to occur in the mantle-crust transition zone (MTZ) dominated by ultramafic/mafic rocks (i.e. lithospheric mantle; Cheng et al., 2020; Li et al., 2002).

The shared geochemical and isotopic features of the El-Shadli mafic and felsic rocks are consistent with a mafic, tholeiitic magma derived from a juvenile mantle source followed by fractionation to more felsic compositions (Figs. 6-8). The El-Shadli felsic rocks have lower Sr and Al_2O_3 and a more pronounced Eu anomaly than the mafic rocks (Supplementary Fig. S3 and Fig. 7), reflecting the important role of plagioclase during fractionation (Li et al., 2002; Stern et al., 1991; Zhang et al., 2017). The lower Ti content of the El-Shadli felsic rocks compared to the mafic rocks indicate fractionation of Ti-Fe oxides (X.-H. Li et al., 2008; Wang et al., 2008) (Fig. 7).

Felsic magmas that fractionated from a parental melt produced by partial melting of a MORB-like mafic source should yield (a) a flat or slightly decreasing REE trend with increasing SiO_2, and (b) slightly higher and/or overlapping REE patterns with coexisting mafic rocks (Brophy, 2009). In contrast, felsic rocks produced through direct fractional crystallization of a primary mantle melt should yield a positive correlation between REE and SiO_2 over the entire mafic to the felsic range (Brophy, 2009). The El-Shadli mafic and felsic rocks have flat REE patterns with some overlap (Fig. 7) and no correlation between La vs. SiO_2 (Fig. 14c) consistent with a partial melting origin of a MORB-like mafic source to produce the mafic magma that later fractionated to felsic ones (Fig. 14). This process is in contrast with that of the Iceland lavas, thought to have been formed through fractional crystallization from mantle-derived tholeiitic basalt and display a positive La-SiO_2 correlation with a steady increase in La content from mafic to felsic end-members (Brophy, 2009).

The low $\delta^{18}O$ values of zircons in the felsic rocks (4.50 ± 0.18 and 5.24 ± 0.18 ‰ (Fig. 11b) can be explained either by re-melting of hydrothermally altered source rocks or by assimilation by the magma of hydrothermally altered wall rock during magma emplacement (Grimes et al., 2013; H. Wang et al., 2016). If the El-Shadli felsic magma underwent assimilation, it should contain zircon xenocrysts and Hf-O isotopic data with upper crustal compositions (Kemp et al., 2007; H. Wang et al., 2016), neither of which have been observed (Fig. 11b). Also, typical $\delta^{18}O$ depth profiles of normal oceanic lithosphere show $\delta^{18}O$ values of lower crustal MTZ gabbroic and ultramafic rocks as low as 2 ‰, reflecting an interaction with high-temperature seawater-derived/hydrothermal fluids, which is common in such settings (Bindeman, 2008; Eiler, 2001; Grimes et al., 2013; Stakes and Taylor, 2003). High-temperature hydrothermal fluids (i.e., seawater) can interact with the oceanic lower crust down to upper mantle levels (Tao et al., 2020). Taken together, the high $\varepsilon Hf_{(t)}$ values and the slightly lower $\delta^{18}O$ values in zircon (Fig. 11) are similar to the isotopic features of older mafic/ultramafic lower oceanic crust (H. Wang et al., 2016) (Fig. 11b), suggesting that the felsic rocks of the El-Shadli bimodal suite likely originated from fractional crystallization of a mafic melt produced by partial melting of MTZ rocks of the lower oceanic crust.

In summary, the El-Shadli bimodal suite formed from the same parental source; the mafic magmas with MORB-like composition fractionated from a parental melt created by partial melting of hydrothermally altered MTZ rocks (i.e. oceanic lithosphere) that finally fractionated to yield more felsic compositions.

5.3. Origin of the El-Shadli intermediate rocks

As mentioned above, field observations show that the volumetrically minor intermediate rocks intruded the El-Shadli mafic rocks (Fig. 4h, i). They are distinct from mafic and felsic rocks in the whole-rock geochemistry, Nd-Sr isotopic data, and U-Pb-Hf-O zircon compositions. The following lines of evidence suggest that the El-Shadli intermediate rocks were derived from an arc-like parental magma. First, these intermediate rocks have high K_2O contents (> 1 wt. %) and their trace element contents and ratios (e.g., Th, Co, Th/Yb, and Zr/Y) are typical of rocks with a calc-alkaline affinity (Fig. 6d-f). In Figure 7c, the intermediate rocks show enrichment in LILE (e.g., Cs, Ba, Th, Pb, and U) and LREE (e.g., La and Ce) relative to HFSE (e.g., Nb, Zr, and Ti), which is typical of a source that underwent melt/fluid interaction during subduction (Gamal El Dien et al., 2020, 2019; Kessel et al., 2005; Pearce and Peate, 1995; Pearce and Reagan, 2019; X.-C. Wang et al., 2016). As a result of these traits, intermediate rocks plot in arc-like fields on standard tectonic discrimination diagrams (Fig. 13).

Second, the two intermediate rock samples have negative εNd (-3.57 and -4.91) and low εNd(t) (+1.38 and –1.04) values which, in conjunction with the litho-geochemical data, indicate the interaction of the parental magma with crustal and/or sedimentary materials, most likely in an arc setting (Gamal El Dien et al., 2020; Li et al., 2019; Pearce and Peate, 1995; Togashi et al., 1992) (Figs. 8 and 14a). Finally, zircon U-Pb analyses of andesitic sample S16 indicate the presence of a zircon xenocryst (#S16@4; Fig. 9d), which indicates contamination of the parental magma by crustal components. The high U/Yb (mostly > 0.1) of these zircons is also characteristic of arc-generated zircons (Carley et al., 2014; Grimes et al., 2015, 2007) (Fig. 10). Taking into account the above-mentioned arc signature and the slightly lower Hf and O isotopic values in zircon that likely preserve the older lower crust features (H. Wang et al., 2016) (Fig. 11), these intermediate rocks may have originated from partial melting of arc-related lower oceanic crust, modified by subduction (i.e. metasomatized; Figs. 10 and 14b).

5.4. Formation mechanism and tectonic implications

Field observations and whole-rock/zircon geochemical and isotopic data suggest that the El-Shadli volcanic province formed in a rift environment, not in a volcanic arc (Stern et al., 1991) (Figs. 3, 7, 8, 10, 12, and 13). Nonetheless, rifting due to regional extension can occur either in a back-arc environment or in a non-arc-related continental rifting environment (Tatsumi and Kimura, 1991).

A back-arc extension model implies a genetic association with subduction (Brooks et al., 1984; Ohki et al., 1994; Pearce et al., 2005; Tang et al., 2014; Tatsumi and Kimura, 1991; Taylor and Martinez, 2003). However, the geochemical characteristics of the El-Shadli bimodal volcanics argue against such an association. Bimodal volcanism generated in back-arc settings is characterized by the presence of subduction zone geochemical signatures in both mafic and felsic compositions. For example, magmatism in Western Pacific back-arc basins (Ohki et al., 1994; Pearce et al., 2005; Shinjo et al., 1999; Shinjo and Kato, 2000; Tang et al.,

2014) is characterized by high LREE contents with $(La/Sm)_{CI}$ = 2–4 and $(La/Yb)_{CI}$ = 2–5 (Shinjo et al., 1999; Shinjo and Kato, 2000). In contrast, the LREE depletion and lack of LILE enrichment are atypical of back-arc mafic rocks. Felsic rocks in back-arc extension settings typically have medium-K contents (~2–3 wt. %; Shinjo and Kato, 2000), in contrast to the low-K contents (<1 wt. %) of the El-Shadli bimodal suite (Fig. 6d). Isotopic data suggesting a highly depleted source for the El-Shadli bimodal suite argues against a back-arc environment which typically reflects derivation from an enriched sub-arc mantle (Bézos et al., 2009; Espinoza et al., 2008; Li et al., 2016; Ohki et al., 1994; Pearce et al., 2005; Shinjo et al., 1999; Shinjo and Kato, 2000; Tang et al., 2014; Taylor and Martinez, 2003; Wei et al., 2017).

The absence of significant deformation and metamorphism in the El-Shadli volcanics is consistent with their emplacement within a relatively stable within-plate/ rift-related tectonic setting (Stern et al., 1991). The volcanics, along with the older and likely underlying granitoids (~730-720 Ma: Gamal El Dien et al., under review) which intrude the strongly deformed and metamorphosed older ophiolitic complexes (~740 Ma; Fig. 2) (Abdel El-Wahed et al., 2019; Fowler and Hamimi, 2021; Youssef et al., 2000), are interpreted to have formed in a post-accretional and rift-related tectonic setting.

The N-MORB geochemical and isotopic signatures indicate the parental mafic magma was likely derived from partial melting of the juvenile mantle during a rifting event. The timing of the magmatism occurred within the time interval dominated by global-scale rifting and break-up of the supercontinent Rodinia (~825–600 Ma; Li et al., 2013; Z. X. Li et al., 2008). This breakup is thought to have been driven either by extension resulted from subduction retreat around the periphery of Rodinia (Cawood et al., 2016, 2009), or by mantle plumes (Li et al., 2013; Z. X. Li et al., 2008; Li and Zhong, 2009). Given that (i) the ANS formed by terrane accretion (Fritz et al., 2013; Stern, 1994), and (ii) geologic evidence suggests that the El Shadli bimodal suite formed in a post-accretionary setting, the ca. 700 Ma El-Shadli rifting event was most likely driven by mantle upwelling induced either by slab break-off following the accretion of the southern Eastern Desert and Gebeit/Gagbaba terranes along the Allaqi-Sol Hamed suture zone between ~800 and 720 Ma (Ali et al., 2010; Fritz et al., 2013; Johnson et al., 2011) or by a mantle plume emanating from the periphery of the Rodinia superplume (Li et al., 2013; Z. X. Li et al., 2008; Li and Zhong, 2009).

The plume-induced model is preferred here based on the following arguments. The El-Shadli volcanic province is the largest bimodal volcanic suite in the Eastern Desert, and possibly in all of the ANS terranes, with an area of 80 km x 35 km and thickness of > 10 km (Khudeir et al., 1988; Shukri and Mansour, 1980; Stern et al., 1991). Given this exceptional thickness and large lateral dimension, an enormous amount of heat (e.g., mantle plumes) would be required to remelt such a large volume of the depleted mafic/ultramafic MTZ rocks (oceanic lithosphere), i.e. reworking of a juvenile crust. This interpretation is consistent with the model proposed by Stern et al. (1991) in which the province was formed during extensive lithospheric extension and high-temperature melting that might have been driven by a plume. Evidence for coeval mantle plume activity in the region includes (1) plume magma additions such as (a) the 710 ± 7 Ma G. Dahanib komatiitic layered mafic-ultramafic intrusions (Fig. 1b; Dixon, 1981) located along the southern margin of the El-Shadli volcanic province (dated at 698 ± 6 Ma; this study) and (b) the 741 ± 24 Ma Korab Kansi ferropicritic layered mafic-ultramafic intrusions (Fig. 1b; Khedr et al., 2020) located in the southern part of the El-Shadli volcanic province; and (2) the apparent hiatus between the ~730-722 Ma granitoids and the ~700 Ma El-Shadli volcanics which may represent plume-induced syn-magmatic doming and denudation as reported in Neoproterozoic South China (Li et al., 1999).

It can thus be argued that mantle plume started in this region at ~ 740 Ma and lasted until ~700 Ma, which is in agreement with the location of the ANS in Rodinia reconstruction at this time along the edge of the Rodinia superplume (Li et al., 2013; Z. X. Li et al., 2008; Li and Zhong, 2009). Geodynamic models (e.g., Burke et al., 2008) imply that plumes preferentially emanate from the margins of superplumes. Thus, the plume that caused the rifting of the ANS here could have formed at the margin of the Rodinia superplume. In addition, the accretion of oceanic lithosphere (ophiolites) and arc crust that formed the ANS proto-crust also occurred along the edge of Rodinia (Li et al., 2013; Z. X. Li et al., 2008) facing an external (the Mozambique Ocean), rather than an internal ocean formed during Rodinia's break-up (Li et al., 2013; Z. X. Li et al., 2008). We thus envisage that the previously accreted proto-crust of the ANS (including the Eastern Desert, Midyan, Gabgaba, and Gebeit terranes) (Fig. 15a, b) was reworked by a mantle plume related to Rodinia break-up (Fig. 15c).

The ~825–600 Ma rifting and fragmentation of Rodinia has been associated with different plume-related magmatic events producing igneous rocks including granitoids, mafic and ultramafic dikes, rift-related bimodal volcanics, and rare komatiitic basalts (Cheng et al., 2020; Frimmel et al., 2002; Heaman et al., 1992; X. H. Li et al., 2003; Li et al., 1999; Z. X. Li et al., 2008, 2003; Lyu et al., 2017; Wang et al., 2007; Zhang et al., 2006). The field and geochemical characteristics of the El-Shadli bimodal volcanics show similarity with other Neoproterozoic rift-related volcanics believed to have formed above mantle plumes (Cheng et al., 2020; Frimmel et al., 2002; Heaman et al., 1992; X. H. Li et al., 2003; Li et al., 1999; Z. X. Li et al., 2008, 2003; Lyu et al., 2017; Wang et al., 2007; Zhang et al., 2006). The presence of rare intermediate rocks in the El-Shadli volcanic province is interpreted to represent partial melting of metasomatized, low-K lower crust of an accreted arc (Fig. 15).

To summarise, in our preferred tectonic model (Fig. 15), both the ~730–722 Ma granitoids-gabbro association (Gamal El Dien et al., under review) and the ~700 Ma El-Shadli bimodal volcanic suite represent successive remelting products of oceanic lithosphere newly accreted to the ANS. Our work highlights the importance of mantle plume events in the consolidation and stratification of the newly accreted ANS Neoproterozoic juvenile terranes to form normal chemically stratified continental crust through intensive lithospheric remelting and crustal reworking, likely accompanied by new melt additions from the mantle.

Acknowledgments

We would like to thank Dr. Allen Kennedy and Mr. Hao Gao for helping in operating the SHRIMP and data reduction, Ms. Elaine Miller for assisting with CL imaging, and Mr. Brad McDonald for assistance with LA-ICP-MS analyses of zircon. We are greatly indebted to Dr. Josh Beardmore for proofreading. We thank the associate editor Dr. Kamal Ali and two anonymous reviewers for their constructive comments. This work was supported by the Australian Research Council Laureate Fellowship grant to Z.-X.L. (FL150100133). Research in the John de Laeter Centre GeoHistory Facility is enabled by AuScope (auscope.org.au) and the Australian Government via the National Collaborative Research Infrastructure Strategy (NCRIS). The NPII multi-collector was obtained via funding from the Australian Research Council LIEF program (LE150100013). This is a contribution to IGCP 648: Supercontinent Cycles and Global Geodynamics.

6. References

Abd El-Rahman, Y., Abu Anbar, M., Li, X.-H., Li, J., Ling, X.-X., Wu, L.-G., Masoud, A.E., 2019. The evolution of the Arabian-Nubian Shield and survival of its zircon U-Pb-Hf-O isotopic signature: A tale from the Um Had Conglomerate, central Eastern Desert, Egypt. Precambrian Res. 320, 46–62. https://doi.org/10.1016/J.PRECAMRES.2018.10.011

Abd El-Rahman, Y., Polat, A., Dilek, Y., Fryer, B., El-Sharkawy, M., Sakran, S., 2009a. Geochemistry and tectonic evolution of the Neoproterozoic Wadi Ghadir ophiolite, Eastern Desert, Egypt. Lithos 113, 158–178. https://doi.org/10.1016/j.lithos.2008.12.014

Abd El-Rahman, Y., Polat, A., Dilek, Y., Fryer, B.J., El-Sharkawy, M., Sakran, S., 2009b. Geochemistry and tectonic evolution of the Neoproterozoic incipient arc-forearc crust in the Fawakhir area, Central Eastern Desert of Egypt. Precambrian Res. 175, 116–134. https://doi.org/10.1016/j.precamres.2009.09.008

Abd El-Rahman, Y., Seifert, T., Gutzmer, J., Said, A., Hofmann, M., Gärtner, A., Linnemann, U., 2017. The South Um Mongul Cu-Mo-Au prospect in the Eastern Desert of Egypt: From a mid-Cryogenian continental arc to Ediacaran post-collisional appinite-high Ba-Sr monzogranite. Ore Geol. Rev. 80, 250–266. https://doi.org/10.1016/J.OREGEOREV.2016.06.004

Abdel-Karim, A.-A.M., Ali, S., El-Awady, A., Elwan, W., 2019. Mineral and bulk–rock chemistry of Shadli bimodal metavolcanics from Eastern Desert of Egypt: Implication for tectonomagmatic setting and Neoproterozoic continental growth in the Arabian–Nubian Shield. Lithos 338–339, 204–217. https://doi.org/10.1016/J.LITHOS.2019.04.026

Abdel-Rahman, A.-F.M., 2019. Geochemistry, age and origin of the Mons Claudianus TTG batholith (Egypt): insight into the role of Pan-African magmatism in uniting plates of Gondwana. Geol. Mag. 1–20. https://doi.org/10.1017/S0016756818000304

Abdel El-Wahed, M., Kamh, S.Z., Ashmawy, M., Shebl, A., 2019. Transpressive Structures in the Ghadir Shear Belt, Eastern Desert, Egypt: Evidence for Partitioning of Oblique Convergence in the Arabian- Nubian Shield during Gondwana Agglutination. Acta Geol. Sin. - English Ed. 93, 1614–1646. https://doi.org/10.1111/1755-6724.13882

Akaad, M., El-Ramly, M., 1960. Geological history and classification of the basement rocks of the Central Eastern Desert of Egypt. Geol. Surv. Egypt 9, 1–15.

Akaad, M., Noweir, A., 1969. Lithostratigraphy of the Hammamat-Umm Seleimat district, Eastern Desert, Egypt. Nature 233, 284–285.

Ali, K.A., Andresen, A., Manton, W.I., Stern, R.J., Omra, S.A., Maurice, A.E., 2012a. U–Pb zircon dating and Sr–Nd–Hf isotopic evidence to support a juvenile origin of the ~ 634 Ma El Shalul granitic gneiss dome, Arabian–Nubian Shield. Geol. Mag. 149, 783–797. https://doi.org/10.1017/S0016756811000975

Ali, K.A., Azer, M.K., Gahlan, H.A., Wilde, S.A., Samuel, M.D., Stern, R.J., 2010. Age constraints on the formation and emplacement of Neoproterozoic ophiolites along the Allaqi-Heiani Suture, South Eastern Desert of Egypt. Gondwana Res. 18, 583–595. https://doi.org/10.1016/j.gr.2010.03.002

Ali, K.A., Kröner, A., Hegner, E., Wong, J., Li, S.-Q., Gahlan, H.A., Abu El Ela, F.F., 2015. U–Pb zircon geochronology and Hf–Nd isotopic systematics of Wadi Beitan granitoid gneisses, South Eastern Desert, Egypt. Gondwana Res. 27, 811–824. https://doi.org/10.1016/J.GR.2013.11.002

Ali, K.A., Moghazi, A.-K.M., Maurice, A.E., Omar, S.A., Wang, Q., Wilde, S.A., Moussa, E.M., Manton, W.I., Stern, R.J., 2012b. Composition, age, and origin of the ~620 Ma Humr Akarim and Humrat Mukbid A-type granites: no evidence for pre-Neoproterozoic basement in the

Eastern Desert, Egypt. Int. J. Earth Sci. 101, 1705–1722. https://doi.org/10.1007/s00531-012-0759-2

Ali, K.A., Stern, R.J., Manton, W.I., Kimura, J.I., Khamees, H.A., 2009. Geochemistry, Nd isotopes and U-Pb SHRIMP zircon dating of Neoproterozoic volcanic rocks from the Central Eastern Desert of Egypt: New insights into the ∼750 Ma crust-forming event. Precambrian Res. 171, 1–22. https://doi.org/10.1016/j.precamres.2009.03.002

Ali, K.A., Wilde, S.A., Stern, R.J., Moghazi, A.K.M., Ameen, S.M.M., 2013. Hf isotopic composition of single zircons from Neoproterozoic arc volcanics and post-collision granites, Eastern Desert of Egypt: Implications for crustal growth and recycling in the Arabian-Nubian Shield. Precambrian Res. 239, 42–55. https://doi.org/10.1016/j.precamres.2013.05.007

Anders, E., Grevesse, N., 1989. Abundances of the elements: Meteoritic and solar. Geochim. Cosmochim. Acta 53, 197–214. https://doi.org/10.1016/0016-7037(89)90286-X

Andresen, A., El-Rus, M.A.A., Myhre, P.I., Boghdady, G.Y., Corfu, F., 2009. U-Pb TIMS age constraints on the evolution of the Neoproterozoic Meatiq Gneiss Dome, Eastern Desert, Egypt. Int. J. Earth Sci. 98, 481–497. https://doi.org/10.1007/s00531-007-0276-x

Arndt, N., Davaille, A., 2013. Episodic Earth evolution. Tectonophysics 609, 661–674. https://doi.org/10.1016/j.tecto.2013.07.002

Arndt, N.T., 2013. Formation and evolution of the continental crust. Geochemical Perspect. 2. https://doi.org/10.7185/geochempersp.2.3

Augland, L.E., Andresen, A., Boghdady, G.Y., 2012. U–Pb ID-TIMS dating of igneous and metaigneous rocks from the El-Sibai area: time constraints on the tectonic evolution of the Central Eastern Desert, Egypt. Int. J. Earth Sci. 101, 25–37. https://doi.org/10.1007/s00531-011-0653-3

Basta, F.F., Maurice, A.E., Bakhit, B.R., Ali, K.A., Manton, W.I., 2011. Neoproterozoic contaminated MORB of Wadi Ghadir ophiolite, NE Africa: Geochemical and Nd and Sr isotopic constraints. J. African Earth Sci. 59, 227–242. https://doi.org/10.1016/j.jafrearsci.2010.10.008

Belousova, E., Griffin, W., O'Reilly, S.Y., Fisher, N., 2002. Igneous zircon: trace element composition as an indicator of source rock type. Contrib. to Mineral. Petrol. 143, 602–622. https://doi.org/10.1007/s00410-002-0364-7

Belousova, E.A., Jiménez, J.M.G., Graham, I., Griffin, W.L., O'Reilly, S.Y., Pearson, N., Martin, L., Craven, S., Talavera, C., 2015. The enigma of crustal zircons in upper-mantle rocks: Clues from the Tumut ophiolite, Southeast Australia. Geology 43, 119–122. https://doi.org/10.1130/G36231.1

Belousova, E.A., Kostitsyn, Y.A., Griffin, W.L., Begg, G.C., O'Reilly, S.Y., Pearson, N.J., 2010. The growth of the continental crust: Constraints from zircon Hf-isotope data. Lithos 119, 457–466. https://doi.org/10.1016/J.LITHOS.2010.07.024

Bentor, Y.K., 1985. The crustal evolution of the Arabo-Nubian Massif with special reference to the Sinai Peninsula. Precambrian Res. 28, 1–74. https://doi.org/10.1016/0301-9268(85)90074-9

Bézos, A., Escrig, S., Langmuir, C.H., Michael, P.J., Asimow, P.D., 2009. Origins of chemical diversity of back-arc basin basalts: A segment-scale study of the Eastern Lau Spreading Center. J. Geophys. Res. 114, B06212–B06212. https://doi.org/10.1029/2008JB005924

Bindeman, I., 2008. Oxygen isotopes in mantle and crustal magmas as revealed by single crystal analysis. Rev. Mineral. Geochemistry 69, 445–478. https://doi.org/10.2138/rmg.2008.69.12

Bonin, B., 2007. A-type granites and related rocks: Evolution of a concept, problems and prospects. Lithos 97, 1–29. https://doi.org/10.1016/J.LITHOS.2006.12.007

Breitkreuz, C., Eliwa, H., Khalaf, I., Gameel, K. El, Bühler, B., Sergeev, S., Larionov, A., Murata, M., 2010. Neoproterozoic SHRIMP U–Pb zircon ages of silica-rich Dokhan Volcanics in the North Eastern Desert, Egypt. Precambrian Res. 182, 163–174. https://doi.org/10.1016/J.PRECAMRES.2010.06.019

Brooks, D.A., Carlson, R.L., Harry, D.L., Melia, P.J., Moore, R.P., Rayhorn, J.E., Tube, S.G., 1984. Characteristics of back-arc regions. Tectonophysics 102, 1–16. https://doi.org/10.1016/0040-1951(84)90005-2

Brophy, J.G., 2009. La-sio2and Yb-SiO2 systematics in mid-ocean ridge magmas: Implications for the origin of oceanic plagiogranite. Contrib. to Mineral. Petrol. 158, 99–111. https://doi.org/10.1007/s00410-008-0372-3

Bühler, B., Breitkreuz, C., Pfänder, J.A., Hofmann, M., Becker, S., Linnemann, U., Eliwa, H.A., 2014. New insights into the accretion of the Arabian-Nubian Shield: Depositional setting, composition and geochronology of a Mid-Cryogenian arc succession (North Eastern Desert, Egypt). Precambrian Res. 243, 149–167. https://doi.org/10.1016/j.precamres.2013.12.012

Burke, K., Steinberger, B., Torsvik, T.H., Smethurst, M.A., 2008. Plume Generation Zones at the margins of Large Low Shear Velocity Provinces on the core-mantle boundary. Earth Planet. Sci. Lett. 265, 49–60. https://doi.org/10.1016/j.epsl.2007.09.042

Carley, T.L., Miller, C.F., Wooden, J.L., Padilla, A.J., Schmitt, A.K., Economos, R.C., Bindeman, I.N., Jordan, B.T., 2014. Iceland is not a magmatic analog for the Hadean: Evidence from the zircon record. Earth Planet. Sci. Lett. 405, 85–97. https://doi.org/10.1016/j.epsl.2014.08.015

Cawood, P.A., Kröner, A., Collins, W.J., Kusky, T.M., Mooney, W.D., Windley, B.F., 2009. Accretionary orogens through Earth history. Geol. Soc. Spec. Publ. 318, 1–36. https://doi.org/10.1144/SP318.1

Cawood, P.A., Strachan, R.A., Pisarevsky, S.A., Gladkochub, D.P., Murphy, J.B., 2016. Linking collisional and accretionary orogens during Rodinia assembly and breakup: Implications for models of supercontinent cycles. Earth Planet. Sci. Lett. 449, 118–126. https://doi.org/10.1016/J.EPSL.2016.05.049

Cheng, J.X., Li, W.X., Wang, X.C., Li, X.H., Pang, C.J., 2020. Petrogenesis of ca. 830 Ma Lushan bimodal volcanic rocks at the southeastern margin of the Yangtze Block, South China: Implications for asthenospheric upwelling and reworking of juvenile crust. Precambrian Res. 342, 105673. https://doi.org/10.1016/j.precamres.2020.105673

Dhuime, B., Hawkesworth, C.J., Cawood, P.A., Storey, C.D., 2012. A change in the geodynamics of continental growth 3 billion years ago. Science (80). 335, 1334–1336. https://doi.org/10.1126/science.1216066

Dhuime, B., Hawkesworth, C.J., Delavault, H., Cawood, P.A., 2018. Rates of generation and destruction of the continental crust: Implications for continental growth, in: Philosophical Transactions of the Royal Society A: Mathematical, Physical and Engineering Sciences. Royal Society Publishing. https://doi.org/10.1098/rsta.2017.0403

Dixon, T.H., 1981. Gebel Dahanib, Egypt: A Late Precambrian Layered Sill of Komatiitic Composition T.H. Contrib. to Mineral. Petrol. Miner. Pet. 76, 42–52.

Eiler, J.M., 2001. Oxygen isotope variations of basaltic lavas and upper mantle rocks. Rev. Mineral. Geochemistry 43, 319–364. https://doi.org/10.2138/gsrmg.43.1.319

El-Bialy, M.Z., Eliwa, H.A., Mahdy, N.M., Murata, M., El-Gameel, K.H., Sehsah, H., Omar, M., Kato, Y., Fujinaga, K., Andresen, A., Thomsen, T.B., 2020. U-Pb zircon geochronology and geochemical constraints on the Ediacaran continental arc and post-collision Granites of Wadi Hawashiya, North Eastern Desert, Egypt: Insights into the ~600 Ma crust-forming Event in the northernmost part of Arabian-Nubian Shield. Precambrian Res. 345, 105777. https://doi.org/10.1016/j.precamres.2020.105777

El-Gaby, S., El-Nady, O., 1984. Tectonic Evolution of the Basement Complex in the Central Eastern Desert of Egypt. Geol. Rundschau 73, 1019–1036.

El-Sayed, M.M., Furnes, H., Mohamed, F.H., 1999. Geochemical constraints on the tectonomagmatic evolution of the late Precambrian Fawakhir ophiolite, Central Eastern Desert, Egypt. J. African Earth Sci. 29, 515–533. https://doi.org/10.1016/S0899-5362(99)00113-X

El-Shazly, S.M., El-Sayed, M.M., 2000. Petrogenesis of the Pan-African El-Bula igneous suite, central Eastern Desert, Egypt. J. African Earth Sci. 31, 317–336. https://doi.org/10.1016/S0899-5362(00)00101-9

Eliwa, H A, Breitkreuz, C., Murata, M., Khalaf, I.M., Bühler, B., Itaya, T., Takahashi, T., Hirahara, Y., Miyazaki, T., Kimura, J.-I., Shibata, T., Koshi, Y., Kato, Y., Ozawa, H., Daas, M.A., El Gameel, K., 2014. SIMS zircon U–Pb and mica K–Ar geochronology, and Sr–Nd isotope geochemistry of Neoproterozoic granitoids and their bearing on the evolution of the north Eastern Desert, Egypt. Gondwana Res. 25, 1570–1598. https://doi.org/10.1016/J.GR.2013.06.006

Eliwa, Hassan A, El-Bialy, M.Z., Murata, M., 2014. Edicaran post-collisional volcanism in the Arabian-Nubian Shield: The high-K calc-alkaline Dokhan Volcanics of Gabal Samr El-Qaa (592 ± 5 Ma), North Eastern Desert, Egypt. Precambrian Res. 246, 180–207. https://doi.org/10.1016/J.PRECAMRES.2014.03.015

Eliwa, H.A., Kimura, J.I., Itaya, T., 2006. Late Neoproterozoic Dokhan Volcanics, North Eastern Desert, Egypt: Geochemistry and petrogenesis. Precambrian Res. 151, 31–52. https://doi.org/10.1016/j.precamres.2006.08.005

Ernst, R., Bleeker, Wouter, Bleeker, W, 2010. Large igneous provinces (LIPs), giant dyke swarms, and mantle plumes: significance for breakup events within Canada and adjacent regions from 2.5 Ga to the Present. Can. J. Earth Sci 47, 695–739. https://doi.org/10.1139/E10-025

Ernst, R.E., Buchan, K.L., 2001. The use of mafic dike swarms in identifying and locating mantle plumes. Spec. Pap. 352 Mantle plumes their Identif. through time 247–265. https://doi.org/10.1130/0-8137-2352-3.247

Espinoza, F., Morata, D., Polvé, M., Lagabrielle, Y., Maury, R.C., Guivel, C., Cotten, J., Bellon, H., Suárez, M., 2008. Bimodal back-arc alkaline magmatism after ridge subduction: Pliocene felsic rocks from Central Patagonia (47°S). Lithos 101, 191–217. https://doi.org/10.1016/j.lithos.2007.07.002

Faisal, M., Yang, X., Khalifa, I.H., Amuda, A.K., Sun, C., 2020. Geochronology and geochemistry of Neoproterozoic Hamamid metavolcanics hosting largest volcanogenic massive sulfide deposits in Eastern Desert of Egypt: Implications for petrogenesis and tectonic evolution. Precambrian Res. 344, 105751. https://doi.org/10.1016/j.precamres.2020.105751

Fowler, A.R., Hamimi, Z., 2021. A review and synthesis of strain studies in the Egyptian Nubian Shield: materials, methods, problems and prospects. Precambrian Res. 355, 106072. https://doi.org/10.1016/j.precamres.2020.106072

Frimmel, H.E., Zartman, R.E., Späth, A., 2002. The Richtersveld Igneous Complex, South Africa: U- Pb Zircon and Geochemical Evidence for the Beginning of Neoproterozoic Continental Breakup. J. Geol. 109, 493–508. https://doi.org/10.1086/320795

Fritz, H., Abdelsalam, M., Ali, K.A., Bingen, B., Collins, A.S., Fowler, A.R., Ghebreab, W., Hauzenberger, C.A., Johnson, P.R., Kusky, T.M., Macey, P., Muhongo, S., Stern, R.J., Viola, G., 2013. Orogen styles in the East African Orogen: A review of the Neoproterozoic to

Cambrian tectonic evolution. J. African Earth Sci. 86, 65–106. https://doi.org/10.1016/j.jafrearsci.2013.06.004

Frost, B.R., Barnes, C.G., Collins, W.J., Arculus, R.J., Fllis, D.J., Frost, C.D., 2001. A Geochemical Classification for Granitic Rocks. J. Petrol. 42, 2033–2048. https://doi.org/10.1093/petrology/42.11.2033

Furnes, H., De Wit, M., Dilek, Y., 2014. Four billion years of ophiolites reveal secular trends in oceanic crust formation. Geosci. Front. 5, 571–603. https://doi.org/10.1016/j.gsf.2014.02.002

Gamal El Dien, H., Li, Z.-X., Abu Anbar, M., Doucet, L.S., Murphy, J. B., Noreen, E., Xia, X., Li, J. 2021. The largest plagiogranite on Earth formed by re-melting of juvenile continental crust. Under review.

Gamal El Dien, H., Doucet, L.S., Murphy, J.B., Li, Z.-X., 2020. Geochemical evidence for a widespread mantle re-enrichment 3.2 billion years ago: implications for global-scale plate tectonics. Sci. Rep. 10. https://doi.org/10.1038/s41598-020-66324-y

Gamal El Dien, H., Hamdy, M., Abu El-Ela, A.S., Abu-Alam, T., Hassan, A., Kil, Y., Mizukami, T., Soda, Y., 2016. Neoproterozoic serpentinites from the Eastern Desert of Egypt: Insights into Neoproterozoic mantle geodynamics and processes beneath the Arabian-Nubian Shield. Precambrian Res. 286. https://doi.org/10.1016/j.precamres.2016.10.006

Gamal El Dien, H., Hamdy, M., El-Ela, A.S.A., Hassan, A., Kil, Y., 2015. A Window into Neoproterozoic Mantle and its Development: Observations from Ophiolitic Serpentinites in the Eastern Desert of Egypt. Acta Geol. Sin. - English Ed. 89, 22–24. https://doi.org/10.1111/1755-6724.12308_16

Gamal El Dien, H., Li, Z.-X., Kil, Y., Abu-Alam, T., 2019. Origin of arc magmatic signature: A temperature-dependent process for trace element (re)-mobilization in subduction zones. Sci. Rep. 9, 7098. https://doi.org/10.1038/s41598-019-43605-9

Griffin, W.L., Wang, X., Jackson, S.E., Pearson, N.J., O'Reilly, S.Y., Xu, X., Zhou, X., 2002. Zircon chemistry and magma mixing, SE China: In-situ analysis of Hf isotopes, Tonglu and Pingtan igneous complexes. Lithos 61, 237–269. https://doi.org/10.1016/S0024-4937(02)00082-8

Grimes, C.B., John, B.E., Kelemen, P.B., Mazdab, F.K., Wooden, J.L., Cheadle, M.J., Hanghøj, K., Schwartz, J.J., 2007. Trace element chemistry of zircons from oceanic crust: A method for distinguishing detrital zircon provenance. Geology 35, 643–646. https://doi.org/10.1130/G23603A.1

Grimes, C.B., Ushikubo, T., Kozdon, R., Valley, J.W., 2013. Perspectives on the origin of plagiogranite in ophiolites from oxygen isotopes in zircon. Lithos 179, 48–66. https://doi.org/10.1016/j.lithos.2013.07.026

Grimes, C.B., Wooden, J.L., Cheadle, M.J., John, B.E., 2015. "Fingerprinting" tectono-magmatic provenance using trace elements in igneous zircon. Contrib. to Mineral. Petrol. 170, 1–26. https://doi.org/10.1007/s00410-015-1199-3

Hamdy, M.M., Abd El-Wahed, M.A., Gamal El Dien, H., Morishita, T., 2017. Garnet hornblendite in the Meatiq Core Complex, Central Eastern Desert of Egypt: Implications for crustal thickening preceding the ~600 Ma extensional regime in the Arabian-Nubian Shield. Precambrian Res. 298. https://doi.org/10.1016/j.precamres.2017.07.002

Hastie, A.R., Kerr, A.C., Pearce, J.A., Mitchell, S.F., 2007. Classification of altered volcanic island arc rocks using immobile trace elements: Development of the Th-Co discrimination diagram. J. Petrol. 48, 2341–2357. https://doi.org/10.1093/petrology/egm062

Hawkesworth, C., Cawood, P., Dhuime, B., 2013. Continental growth and the crustal record. Tectonophysics 609, 651–660. https://doi.org/10.1016/j.tecto.2013.08.013

Hawkesworth, C.J., Cawood, P.A., Dhuime, B., 2020. The Evolution of the Continental Crust and the Onset of Plate Tectonics. Front. Earth Sci. 8, 326. https://doi.org/10.3389/feart.2020.00326

Hawkesworth, C.J., Kemp, A.I.S., 2006. Using hafnium and oxygen isotopes in zircons to unravel the record of crustal evolution. Chem. Geol. 226, 144–162. https://doi.org/10.1016/j.chemgeo.2005.09.018

Heaman, L.M., LeCheminant, A.N., Rainbird, R.H., 1992. Nature and timing of Franklin igneous events, Canada: Implications for a Late Proterozoic mantle plume and the break-up of Laurentia. Earth Planet. Sci. Lett. 109, 117–131. https://doi.org/10.1016/0012-821X(92)90078-A

Hofmann, A.W., 2014. Sampling Mantle Heterogeneity through Oceanic Basalts: Isotopes and Trace Elements, in: Treatise on Geochemistry. Elsevier, pp. 67–101. https://doi.org/10.1016/B978-0-08-095975-7.00203-5

Johnson, P.R., Andresen, A., Collins, A.S., Fowler, A.R., Fritz, H., Ghebreab, W., Kusky, T., Stern, R.J., 2011. Late Cryogenian-Ediacaran history of the Arabian-Nubian Shield: A review of depositional, plutonic, structural, and tectonic events in the closing stages of the northern East African Orogen. J. African Earth Sci. 61, 167–232. https://doi.org/10.1016/j.jafrearsci.2011.07.003

Johnson, P.R., Woldehaimanot, B., 2003. Development of the Arabian-Nubian Shield: perspectives on accretion and deformation in the northern East African Orogen and the assembly of Gondwana. Geol. Soc. London, Spec. Publ. 206, 289–325. https://doi.org/10.1144/GSL.SP.2003.206.01.15

Kemp, A.I.S., Hawkesworth, C.J., 2014. Growth and Differentiation of the Continental Crust from Isotope Studies of Accessory Minerals, in: Treatise on Geochemistry. Elsevier, pp. 379–421. https://doi.org/10.1016/B978-0-08-095975-7.00312-0

Kemp, A.I.S., Hawkesworth, C.J., Foster, G.L., Paterson, B.A., Woodhead, J.D., Hergt, J.M., Gray, C.M., Whitehouse, M.J., 2007. Magmatic and crustal differentiation history of granitic rocks from Hf-O isotopes in zircon. Science 315, 980–983. https://doi.org/10.1126/science.1136154

Kemp, A.I.S., Hawkesworth, C.J., Paterson, B.A., Kinny, P.D., 2006. Episodic growth of the Gondwana supercontinent from hafnium and oxygen isotopes in zircon. Nature 439, 580–583. https://doi.org/10.1038/nature04505

Kessel, R., Schmidt, M.W., Ulmer, P., Pettke, T., 2005. Trace element signature of subduction-zone fluids, melts and supercritical liquids at 120–180 km depth. Nature 437, 724–727. https://doi.org/10.1038/nature03971

Khalil, E., 1997. Ocean-arc to continental margin volcanics sequences of the Pan- African Precambrian belt, Egypt: “geochemical approach.” Egypt. J. Geol. 41, 477–528.

Khedr, M.Z., El-Awady, A., Arai, S., Hauzenberger, C., Tamura, A., Stern, R.J., Morishita, T., 2020. Petrogenesis of the ~740 Korab Kansi mafic-ultramafic intrusion, South Eastern Desert of Egypt: Evidence of Ti-rich ferropicritic magmatism. Gondwana Res. 82, 48–72. https://doi.org/10.1016/j.gr.2019.12.013

Khudeir, A., Ali, M., El Habaak, G., 1988. The metavolcanics at Um Samiuku area, Egypt. Bull. Fac. Sci. Assuit Univ. 17, 73–101.

Kinny, P.D., Compston, W., Williams, I.S., 1991. A reconnaissance ion-probe study of hafnium isotopes in zircons. Geochim. Cosmochim. Acta 55, 849–859. https://doi.org/10.1016/0016-7037(91)90346-7

Kinny, P.D., Maas, R., 2003. Lu-Hf and Sm-Nd isotope systems in zircon. Rev. Mineral. Geochemistry 53, 327–341. https://doi.org/10.2113/0530327

Kirkland, C.L., Smithies, R.H., Taylor, R.J.M., Evans, N., McDonald, B., 2015. Zircon Th/U ratios in magmatic environs. Lithos 212–215, 397–414. https://doi.org/10.1016/j.lithos.2014.11.021

Kjøll, H.J., Andersen, T.B., Corfu, F., Labrousse, L., Tegner, C., Abdelmalak, M.M., Planke, S., 2019. Timing of Breakup and Thermal Evolution of a Pre- Caledonian Neoproterozoic Exhumed Magma- Rich Rifted Margin. Tectonics 38, 2018TC005375-2018TC005375. https://doi.org/10.1029/2018TC005375

Koepke, J., Feig, S.T., Snow, J., 2005. Hydrous partial melting within the lower oceanic crust. Terra Nov. 17, 286–291. https://doi.org/10.1111/j.1365-3121.2005.00613.x

Kröner, A., Kruger, J., Rashwan, A.A.A., 1994. Age and tectonic setting of granitoid gneisses in the Eastern Desert of Egypt and south-west Sinai. Geol. Rundschau 83, 502–513. https://doi.org/10.1007/BF00194157

Kröner, A., Linnebacher, P., Stern, R.J., Reischmann, T., Manton, W., Hussein, I.M., 1991. Evolution of Pan-African island arc assemblages in the southern Red Sea Hills, Sudan, and in southwestern Arabia as exemplified by geochemistry and geochronology. Precambrian Res. 53, 99–118. https://doi.org/10.1016/0301-9268(91)90007-W

Kröner, A., Todt, W., Hussein, I.M., Mansour, M., Rashwan, A.A., 1992. Dating of late Proterozoic ophiolites in Egypt and the Sudan using the single grain zircon evaporation technique. Precambrian Res. 59, 15–32. https://doi.org/10.1016/0301-9268(92)90049-T

Lehmann, B., Zoheir, B.A., Neymark, L.A., Zeh, A., Emam, A., Radwan, A.M., Zhang, R., Moscati, R.J., 2020. Monazite and cassiterite U-Pb dating of the Abu Dabbab rare-metal granite, Egypt: Late Cryogenian metalliferous granite magmatism in the Arabian-Nubian Shield. Gondwana Res. 84, 71–80. https://doi.org/10.1016/j.gr.2020.03.001

Li, H.-Y., Taylor, R.N., Prytulak, J., Kirchenbaur, M., Shervais, J.W., Ryan, J.G., Godard, M., Reagan, M.K., Pearce, J.A., 2019. Radiogenic isotopes document the start of subduction in the Western Pacific. Earth Planet. Sci. Lett. 518, 197–210. https://doi.org/10.1016/J.EPSL.2019.04.041

Li, L., Lin, S., Xing, G., Davis, D.W., Jiang, Y., Davis, W., Zhang, Y., 2016. Ca. 830 Ma back-arc type volcanic rocks in the eastern part of the Jiangnan orogen: Implications for the Neoproterozoic tectonic evolution of South China Block. Precambrian Res. 275, 209–224. https://doi.org/10.1016/j.precamres.2016.01.016

Li, W.X., Li, X.H., Li, Z.X., 2010. Ca. 850 Ma bimodal volcanic rocks in northeastern jiangxi province, south china: Initial extension during the breakup of Rodinia? Am. J. Sci. 310, 951–980. https://doi.org/10.2475/09.2010.08

Li, W.X., Li, X.H., Li, Z.X., 2005. Neoproterozoic bimodal magmatism in the Cathaysia Block of South China and its tectonic significance. Precambrian Res. 136, 51–66. https://doi.org/10.1016/j.precamres.2004.09.008

Li, X.-H., Li, W.-X., Li, Z.-X., Liu, Y., 2008. 850–790 Ma bimodal volcanic and intrusive rocks in northern Zhejiang, South China: A major episode of continental rift magmatism during the breakup of Rodinia. Lithos 102, 341–357. https://doi.org/10.1016/J.LITHOS.2007.04.007

Li, X., Li, Z.-X., Zhou, H., Liu, Y., Kinny, P.D., 2002. U–Pb zircon geochronology, geochemistry and Nd isotopic study of Neoproterozoic bimodal volcanic rocks in the Kangdian Rift of South China: implications for the initial rifting of Rodinia. Precambrian Res. 113, 135–154. https://doi.org/10.1016/S0301-9268(01)00207-8

Li, X.H., Li, Z.X., Ge, W., Zhou, H., Li, W., Liu, Y., Wingate, M.T.D., 2003. Neoproterozoic granitoids in South China: Crustal melting above a mantle plume at ca. 825 Ma? Precambrian Res. 122, 45–83. https://doi.org/10.1016/S0301-9268(02)00207-3

Li, Z.X., Bogdanova, S. V, Collins, A.S., Davidson, A., De Waele, B., Ernst, R.E., Fitzsimons, I.C.W., Fuck, R.A., Gladkochub, D.P., Jacobs, J., Karlstrom, K.E., Lu, S., Natapov, L.M., Pease, V., Pisarevsky, S.A., Thrane, K., Vernikovsky, V., 2008. Assembly, configuration, and break-up history of Rodinia: A synthesis. Precambrian Res. 160, 179–210. https://doi.org/10.1016/j.precamres.2007.04.021

Li, Z.X., Evans, D.A.D., Halverson, G.P., 2013. Neoproterozoic glaciations in a revised global palaeogeography from the breakup of Rodinia to the assembly of Gondwanaland. Sediment. Geol. 294, 219–232. https://doi.org/10.1016/j.sedgeo.2013.05.016

Li, Z.X., Li, X.H., Kinny, P.D., Wang, J., 1999. The breakup of Rodinia: did it start with a mantle plume beneath South China? Earth Planet. Sci. Lett. 173, 171–181. https://doi.org/10.1016/S0012-821X(99)00240-X

Li, Z.X., Li, X.H., Kinny, P.D., Wang, J., Zhang, S., Zhou, H., 2003. Geochronology of Neoproterozoic syn-rift magmatism in the Yangtze Craton, South China and correlations with other continents: Evidence for a mantle superplume that broke up Rodinia. Precambrian Res. 122, 85–109. https://doi.org/10.1016/S0301-9268(02)00208-5

Li, Z.X., Zhong, S., 2009. Supercontinent-superplume coupling, true polar wander and plume mobility: Plate dominance in whole-mantle tectonics. Phys. Earth Planet. Inter. 176, 143–156. https://doi.org/10.1016/j.pepi.2009.05.004

Lundmark, A.M., Andresen, A., Hassan, M.A., Augland, L.E., Boghdady, G.Y., 2012. Repeated magmatic pulses in the East African Orogen in the Eastern Desert, Egypt: An old idea supported by new evidence. Gondwana Res. 22, 227–237. https://doi.org/10.1016/j.gr.2011.08.017

Lyu, P.L., Li, W.X., Wang, X.C., Pang, C.J., Cheng, J.X., Li, X.H., 2017. Initial breakup of supercontinent Rodinia as recorded by ca 860–840 Ma bimodal volcanism along the southeastern margin of the Yangtze Block, South China. Precambrian Res. 296, 148–167. https://doi.org/10.1016/j.precamres.2017.04.039

Martin, R.F., Piwinskii, A.J., 1972. Magmatism and tectonic settings. J. Geophys. Res. 77, 4966–4975. https://doi.org/10.1029/jb077i026p04966

Merdith, A.S., Collins, A.S., Williams, S.E., Pisarevsky, S., Foden, J.D., Archibald, D.B., Blades, M.L., Alessio, B.L., Armistead, S., Plavsa, D., Clark, C., Müller, R.D., 2017. A full-plate global reconstruction of the Neoproterozoic. Gondwana Res. 50, 84–134. https://doi.org/10.1016/j.gr.2017.04.001

Middlemost, E.A.K., 1994. Naming materials in the magma/igneous rock system. Earth-Science Rev. 37, 215–224. https://doi.org/10.1016/0012-8252(94)90029-9

Morag, N., Avigad, D., Gerdes, A., Belousova, E., Harlavan, Y., 2011. Crustal evolution and recycling in the northern Arabian-Nubian Shield: New perspectives from zircon Lu–Hf and U–Pb systematics. Precambrian Res. 186, 101–116. https://doi.org/10.1016/J.PRECAMRES.2011.01.004

Morag, N., Avigad, D., Gerdes, A., Harlavan, Y., 2012. 1000–580 Ma crustal evolution in the northern Arabian-Nubian Shield revealed by U–Pb–Hf of detrital zircons from late Neoproterozoic sediments (Elat area, Israel). Precambrian Res. 208–211, 197–212. https://doi.org/10.1016/J.PRECAMRES.2012.04.009

Moussa, E.M.M., Stern, R.J., Manton, W.I., Ali, K.A., 2008. SHRIMP zircon dating and Sm/Nd isotopic investigations of Neoproterozoic granitoids, Eastern Desert, Egypt. Precambrian Res. 160, 341–356. https://doi.org/10.1016/j.precamres.2007.08.006

Niu, Y., O'hara, M.J., 2008. Global Correlations of Ocean Ridge Basalt Chemistry with Axial Depth: a New Perspective. J. Petrol. 49, 633–664. https://doi.org/10.1093/petrology/egm051

Ohki, J., Shuto, K., Kagami, H., 1994. Middle Miocene bimodal volcanism by asthenospheric upwelling: Sr and Nd isotopic evidence from the back-arc region of the Northeast Japan arc. Geochem. J. 28, 473–487. https://doi.org/10.2343/geochemj.28.473

Park, J.K., Buchan, K.L., Harlan, S.S., 1995. A proposed giant radiating dyke swarm fragmented by the separation of Laurentia and Australia based on paleomagnetism of ca. 780 Ma mafic intrusions in western North America. Earth Planet. Sci. Lett. 132, 129–139. https://doi.org/10.1016/0012-821X(95)00059-L

Patchett, P.J., 1983. Importance of the Lu-Hf isotopic system in studies of planetary chronology and chemical evolution. Geochim. Cosmochim. Acta 47, 81–91. https://doi.org/10.1016/0016-7037(83)90092-3

Patchett, P.J., Kouvo, O., Hedge, C.E., Tatsumoto, M., 1981. Evolution of continental crust and mantle heterogeneity: Evidence from Hf isotopes. Contrib. to Mineral. Petrol. 78, 279–297. https://doi.org/10.1007/BF00398923

Pearce, J., 1996. Sources and settings of granitic rocks. Episodes 19, 120–125. https://doi.org/10.18814/epiiugs/1996/v19i4/005

Pearce, J.A., 2008. Geochemical fingerprinting of oceanic basalts with applications to ophiolite classification and the search for Archean oceanic crust. Lithos 100, 14–48. https://doi.org/10.1016/j.lithos.2007.06.016

Pearce, J.A., Harris, N.B.W., Tindle, A.G., 1984. Trace Element Discrimination Diagrams for the Tectonic Interpretation of Granitic Rocks. J. Petrol. 25, 956–983. https://doi.org/10.1093/petrology/25.4.956

Pearce, J.A., Peate, D.W., 1995. Tectonic Implications of Volcanic Arc Magmas. Annu. Rev. Earth Planet. Sci. 23, 251–285.

Pearce, J.A., Reagan, M.K., 2019. Identification, classification, and interpretation of boninites from Anthropocene to Eoarchean using Si-Mg-Ti systematics. Geosphere 15, 1008–1037. https://doi.org/10.1130/GES01661.1

Pearce, J.A., Stern, R.J., Bloomer, S.H., Fryer, P., 2005. Geochemical mapping of the Mariana arc-basin system: Implications for the nature and distribution of subduction components. Geochemistry, Geophys. Geosystems 6. https://doi.org/10.1029/2004GC000895

Pease, V., Johnson, P.R., 2013. Introduction to the JEBEL volume of Precambrian Research. Precambrian Res. 239, 1–5. https://doi.org/10.1016/j.precamres.2013.10.003

Peccerillo, A., Barberio, M.R., Yirgu, G., Ayalew, D., Barbieri, M., Wu, T.W., 2003. Relationships between Maf ic and Peralkaline Silicic Magmatism in Continental Rift Settings: a Petrological, Geochemical and Isotopic Study of the Gedemsa Volcano, Central Ethiopian Rift. J. Petrol. 44, 2003–2032. https://doi.org/10.1093/petrology/egg068

Peccerillo, A., Taylor, S.R., 1976. Geochemistry of eocene calc-alkaline volcanic rocks from the Kastamonu area, Northern Turkey. Contrib. to Mineral. Petrol. 58, 63–81. https://doi.org/10.1007/BF00384745

Polat, A., Hofmann, A.W., 2003. Alteration and geochemical patterns in the 3.7-3.8 Ga Isua greenstone belt, West Greenland, in: Precambrian Research. Elsevier B.V., pp. 197–218. https://doi.org/10.1016/S0301-9268(03)00095-0

Reymer, A., Schubert, G., 1986. Rapid growth of some major segments of continental crust. Geology 14, 299. https://doi.org/10.1130/0091-7613(1986)14<299:RGOSMS>2.0.CO;2

Reymer, A., Schubert, G., 1984. Phanerozoic addition rates to the continental crust and crustal growth. Tectonics 3, 63–77. https://doi.org/10.1029/TC003i001p00063

Robinson, F.A., Foden, J.D., Collins, A.S., Payne, J.L., 2014. Arabian Shield magmatic cycles and their relationship with Gondwana assembly: Insights from zircon U-Pb and Hf isotopes. Earth Planet. Sci. Lett. 408, 207–225. https://doi.org/10.1016/j.epsl.2014.10.010

Rooney, T.O., 2020. The Cenozoic magmatism of East Africa: Part II – Rifting of the mobile belt. Lithos 360–361, 105291. https://doi.org/10.1016/j.lithos.2019.105291

Rooney, T.O., 2017. The Cenozoic magmatism of East-Africa: Part I — Flood basalts and pulsed magmatism. Lithos 286–287, 264–301. https://doi.org/10.1016/J.LITHOS.2017.05.014

Ross, P.-S., Bédard, J.H., 2009. Magmatic affinity of modern and ancient subalkaline volcanic rocks determined from trace-element discriminant diagrams. Can. J. Earth Sci. 46, 823–839. https://doi.org/10.1139/E09-054

Rudnick, R.L., Gao, S., 2014. Composition of the Continental Crust, in: Treatise on Geochemistry. Elsevier, pp. 1–51. https://doi.org/10.1016/B978-0-08-095975-7.00301-6

Shervais, J.W., 1982. TiV plots and the petrogenesis of modern and ophiolitic lavas. Earth Planet. Sci. Lett. 59, 101–118. https://doi.org/10.1016/0012-821X(82)90120-0

Shinjo, R., Chung, S., Kato, Y., Kimura, M., 1999. Geochemical and Sr-Nd isotopic characteristics of volcanic rocks from the Okinawa Trough and Ryukyu Arc: Implications for the evolution of a young, intracontinental back arc basin. J. Geophys. Res. Solid Earth 104, 10591–10608. https://doi.org/10.1029/1999JB900040

Shinjo, R., Kato, Y., 2000. Geochemical constraints on the origin of bimodal magmatism at the Okinawa Trough, an incipient back-arc basin. Lithos 54, 117–137. https://doi.org/10.1016/S0024-4937(00)00034-7

Shukri, N.M., Mansour, M.S., 1980. Lithostratigraphy of Um Samuiki District, Eastern Desert, Egypt, in: Institue Applied Geology, University of Jeddah Bulletin. Elsevier, pp. 83–93. https://doi.org/10.1016/B978-0-08-024481-5.50012-1

Stakes, D.S., Taylor, H.P., 2003. Oxygen isotope and chemical studies on the origin of large plagiogranite bodies in northern Oman, and their relationship to the overlying massive sulphide deposits. Geol. Soc. Spec. Publ. 218, 315–351. https://doi.org/10.1144/GSL.SP.2003.218.01.17

Stein, M., 2003. Tracing the plume material in the Arabian-Nubian Shield. Precambrian Res. 123, 223–234. https://doi.org/10.1016/S0301-9268(03)00069-X

Stein, M., Goldstein, S.L., 1996. From plume head to continental lithosphere in the Arabian–Nubian shield. Nature 382, 773–778. https://doi.org/10.1038/382773a0

Stern, R.J., 2002. Crustal evolution in the East African Orogen: a neodymium isotopic perspective. J. African Earth Sci. 34, 109–117. https://doi.org/10.1016/S0899-5362(02)00012-X

Stern, R.J., 1994. ARC Assembly and Continental Collision in the Neoproterozoic East African Orogen: Implications for the Consolidation of Gondwanaland. Annu. Rev. Earth Planet. Sci. 22, 319–351. https://doi.org/10.1146/annurev.ea.22.050194.001535

Stern, R.J., 1981. Petrogenesis and tectonic setting of late Precambrian ensimatic volcanic rocks, central eastern desert of Egypt. Precambrian Res. 16, 195–230. https://doi.org/10.1016/0301-9268(81)90013-9

Stern, R.J., Hedge, C.E., 1985. Geochronologic and isotopic constraints on late Precambrian crustal evolution in the Eastern Desert of Egypt. Am. J. Sci. 285, 97–127. https://doi.org/10.2475/ajs.285.2.97

Stern, R.J., Johnson, P.R., Kröner, A., Yibas, B., 2004. Neoproterozoic Ophiolites of the Arabian-Nubian Shield. Dev. Precambrian Geol. 13, 95–128. https://doi.org/10.1016/S0166-2635(04)13003-X

Stern, R.J., Kröner, A., Rashwan, A.A., 1991. A late Precambrian (~ 710 Ma) high volcanicity rift in the southern Eastern Desert of Egypt. Geol. Rundschau 80, 155–170. https://doi.org/10.1007/BF01828773

Sun, S. -s., McDonough, W.F., 1989. Chemical and isotopic systematics of oceanic basalts: implications for mantle composition and processes. Geol. Soc. London, Spec. Publ. 42, 313–345. https://doi.org/doi: 10.1144/GSL.SP.1989.042.01.19

Tang, Y., Obayashi, M., Niu, F., Grand, S.P., Chen, Y.J., Kawakatsu, H., Tanaka, S., Ning, J., Ni, J.F., 2014. Changbaishan volcanism in northeast China linked to subduction-induced mantle upwelling. Nat. Geosci. 7, 470–475. https://doi.org/10.1038/ngeo2166

Tao, C., Jr, W.E.S., Lowell, R.P., Liu, Y., Liang, J., Guo, Z., Ding, K., Zhang, H., Liu, J., Qiu, L., Egorov, I., Liao, S., Zhao, M., Zhou, J., Deng, X., Li, H., Wang, H., Cai, W., Zhang, G., Zhou, H., Lin, J., 2020. Deep high-temperature hydrothermal circulation in a detachment faulting system on the ultra-slow spreading ridge. Nat. Commun. 11, 1–9. https://doi.org/10.1038/s41467-020-15062-w

Tatsumi, Y., Kimura, N., 1991. Backarc extension versus continental breakup: petrological aspects for active rifting. Tectonophysics 197, 127–137. https://doi.org/10.1016/0040-1951(91)90037-S

Taylor, B., Martinez, F., 2003. Back-arc basin basalt systematics. Earth Planet. Sci. Lett. 210, 481–497. https://doi.org/10.1016/S0012-821X(03)00167-5

Taylor, S.R., McLennan, S.M., 1995. The geochemical evolution of the continental crust. Rev. Geophys. 33, 241. https://doi.org/10.1029/95RG00262

Togashi, S., Tanaka, T., Yoshida, T., Ishikawa, K., Fujinawa, A., Kurasawa, H., 1992. Trace elements and Nd-Sr isotopes of island arc tholeiites from frontal arc of Northeast Japan. Geochem. J. 26, 261–277. https://doi.org/10.2343/geochemj.26.261

Valley, J.W., 2003. Oxygen Isotopes in Zircon. Rev. Mineral. Geochemistry 53, 343–385. https://doi.org/10.2113/0530343

Valley, J.W., Kinny, P.D., Schulze, D.J., Spicuzza, M.J., 1998. Zircon megacrysts from kimberlite: oxygen isotope variability among mantle melts. Contrib. to Mineral. Petrol. 133, 1–11. https://doi.org/10.1007/s004100050432

Valley, J.W., Lackey, J.S., Cavosie, A.J., Clechenko, C.C., Spicuzza, M.J., Basei, M.A.S., Bindeman, I.N., Ferreira, V.P., Sial, A.N., King, E.M., Peck, W.H., Sinha, A.K., Wei, C.S., 2005. 4.4 billion years of crustal maturation: oxygen isotope ratios of magmatic zircon. Contrib. to Mineral. Petrol. 150, 561–580. https://doi.org/10.1007/s00410-005-0025-8

Vermeesch, P., 2006. Tectonic discrimination diagrams revisited. Geochemistry, Geophys. Geosystems 7, n/a-n/a. https://doi.org/10.1029/2005GC001092

Vervoort, J.D., Blichert-Toft, J., 1999. Evolution of the depleted mantle: Hf isotope evidence from juvenile rocks through time. Geochim. Cosmochim. Acta 63, 533–556. https://doi.org/10.1016/S0016-7037(98)00274-9

Wang, H., Wu, Y.B., Gao, S., Qin, Z.W., Hu, Z.C., Zheng, J.P., Yang, S.H., 2016. Continental growth through accreted oceanic arc: Zircon Hf-O isotope evidence for granitoids from the Qinling orogen. Geochim. Cosmochim. Acta 182, 109–130. https://doi.org/10.1016/j.gca.2016.03.016

Wang, X.-C., Li, X.-H., Li, W.-X., Li, Z.-X., 2007. Ca. 825 Ma komatiitic basalts in South China: First evidence for >1500 °C mantle melts by a Rodinian mantle plume. Geology 35, 1103. https://doi.org/10.1130/G23878A.1

Wang, X.-C., Li, X.-H., Li, W.-X., Li, Z.-X., Liu, Y., Yang, Y.-H., Liang, X.-R., Tu, X.-L., 2008. The Bikou basalts in the northwestern Yangtze block, South China: Remnants of 820-810 Ma continental flood basalts? Geol. Soc. Am. Bull. 120, 1478–1492. https://doi.org/10.1130/B26310.1

Wang, X.-C., Wilde, S.A., Li, Z.-X., Li, S., Li, L., 2020. Do Supercontinent-Superplume Cycles Control the Growth and Evolution of Continental Crust? J. Earth Sci. https://doi.org/10.1007/s12583-020-1077-4

Wang, X.-C., Wilde, S.A., Xu, B., Pang, C.-J., 2016. Origin of arc-like continental basalts: Implications for deep-Earth fluid cycling and tectonic discrimination. Lithos 261, 5–45. https://doi.org/10.1016/j.lithos.2015.12.014

Wei, Y., Zhao, Z., Niu, Y., Zhu, D.C., Liu, D., Wang, Q., Hou, Z., Mo, X., Wei, J., 2017. Geochronology and geochemistry of the Early Jurassic Yeba Formation volcanic rocks in southern Tibet: Initiation of back-arc rifting and crustal accretion in the southern Lhasa Terrane. Lithos 278–281, 477–490. https://doi.org/10.1016/j.lithos.2017.02.013

Whalen, J.B., Currie, K.L., Chappell, B.W., 1987. A-type granites: geochemical characteristics, discrimination and petrogenesis. Contrib. to Mineral. Petrol. 95, 407–419. https://doi.org/10.1007/BF00402202

Whalen, J.B., Hildebrand, R.S., 2019. Trace element discrimination of arc, slab failure, and A-type granitic rocks. Lithos 348–349, 105179. https://doi.org/10.1016/j.lithos.2019.105179

White, W.M., Klein, E.M., 2014. Composition of the Oceanic Crust. Treatise on Geochemistry 457–496. https://doi.org/10.1016/B978-0-08-095975-7.00315-6

Wilde, S.A., Youssed, K., 2002. A re-evaluation of the origin and setting of the Late Precambrian Hammamat Group based on SHRIMP U–Pb dating of detrital zircons from Gebel Umm Tawat, North Eastern Desert, Egypt. J. Geol. Soc. London. 159, 595–604. https://doi.org/10.1144/0016-764901-081

Wilde, S.A., Youssef, K., 2000. Significance of SHRIMP U-Pb dating of the Imperial Porphyry and associated Dokhan Volcanics, Gebel Dokhan, north Eastern Desert, Egypt. J. African Earth Sci. 31, 403–413. https://doi.org/10.1016/S0899-5362(00)00096-8

Winchester, J.A., Floyd, P.A., 1976. Geochemical magma type discrimination: application to altered and metamorphosed basic igneous rocks. Earth Planet. Sci. Lett. 28, 459–469. https://doi.org/10.1016/0012-821X(76)90207-7

Wingate, M.T.D., Campbell, I.H., Compston, W., Gibson, G.M., 1998. Ion microprobe U–Pb ages for Neoproterozoic basaltic magmatism in south-central Australia and implications for the breakup of Rodinia. Precambrian Res. 87, 135–159. https://doi.org/10.1016/S0301-9268(97)00072-7

Youssef, M.M., El-Din, G.M.K., Rashwan, A.A., Akaw, A., 2000. Description and evaluation of shear criteria developed in folds and thrusts of the Wadi El Gemal area, southern Eastern Desert, Egyp, in: 18th Colloquium of African Geology Abstracts. p. 91.

Zhang, C., Koepke, J., France, L., Godard, M., 2017. Felsic Plutonic Rocks from IODP Hole 1256D, Eastern Pacific: Implications for the Nature of the Axial Melt Lens at Fast-Spreading Mid-Ocean Ridges. J. of Petrology 58, 1535–1566. https://doi.org/10.1093/petrology/egx064

Zhang, C.L., Li, Z.X., Li, X.H., Ye, H., Wang, A., Guo, K.Y., 2006. Neoproterozoic bimodal intrusive complex in the southwestern Tarim Block, northwest China: Age, geochemistry, and implications for the rifting of Rodinia. Int. Geol. Rev. 48, 112–128. https://doi.org/10.2747/0020-6814.48.2.112

Zimmer, M., Kröner, A., Jochum, K.P., Reischmann, T., Todt, W., 1995. The Gabal Gerf complex: A precambrian N-MORB ophiolite in the Nubian Shield, NE Africa. Chem. Geol. 123, 29–51. https://doi.org/10.1016/0009-2541(95)00018-H

Figures legend

Fig. 1: (a) A schematic geological map of the Arabian-Nubian Shield showing the distribution of Neoproterozoic terranes and their contact with pre-Neoproterozoic blocks modified after Johnson et al. (2011) and Pease and Johnson (2013). (b) Geological map of the Eastern Desert showing the ages and distribution of the main Precambrian crustal basement rock units. Eastern Desert terrane boundaries are after Stern and Hedge (1985). The map is modified after Johnson et al. (2011).

Fig. 2: Detailed geological map of the studied El-Shadli area showing the ages and distribution of the main rock units: El-Shadli bimodal volcanic rocks, El-Shadli granitoids-diorite-gabbro assemblage, W. Ghadir ophiolitic assemblage, W. Hafafit core complex, post-collision alkaline granites, and post-collisional volcanics. Age data are from Stern et al. (1991), Kröner et al. (1992), Kröner et al. (1994), and Gamal El Dien et al. (under review). The map is modified after the geologic map of Jabal Hamatah quadrangle (GSE, 1997). The black box represents the location of the previous work.

Fig. 3: Field photos for the El-Shadli bimodal volcanic suite showing cyclic intercalation between layers of mafic and felsic rocks at different scales. Red circle highlights the scale.

Fig. 4: Field photos for the El-Shadli bimodal volcanic province. (a) Field photo showing mafic and felsic dykes, interpreted as feeder dykes for the bimodal volcanic province (~700 Ma), that intrude the underlying El-Shadli granitoids (~730 Ma). (b-e) Close-up photos showing the well-developed chilled margins of the mafic dykes (sample S01-2) of up to 1 m width, and their intrusive relationship with the El-Shadli granitoids (sample S01-1a). The granitoids and mafic dykes are both intruded by thin felsic dykes (sample S01-3). The observed field relationships, coupled with geochronological data, suggest that the El-Shadli bimodal volcanics are younger than the El-Shadli granitoids-gabbro association. (f)

Pyroclastic layers intercalation with mafic rocks. (g) Pillow basalts of the mafic end-member. (h-j) intermediate rocks intruding the mafic rocks. (k) Associated agglomerates.

Fig. 5: Photomicrographs of the El Shadli bimodal suite and associated intermediate rocks. (a-f) Cross-polarized light images of the mafic rocks showing the porphyritic, ophitic, and sub-ophitic textures. The primary minerals (plagioclase and clinopyroxene) assemblage are well preserved. (g-j) Cross-polarized light images of the felsic rocks showing porphyritic textures. The phenocrysts include quartz, plagioclase, and potash feldspar. (k-L) Cross-polarized light images of the intermediate rocks showing porphyritic textures and phenocrysts that include quartz, plagioclase, and biotite. Plagioclase= pl, clinopyroxene= cpx, quartz= qz, amphiboles= amph, potash feldspar= kf, biotite= Bi and chlorite= ch.

Fig. 6: Chemical classification diagrams using the whole-rock major and trace element composition of the El-Shadli bimodal volcanic province. (a) Total alkali-silica diagram (TAS) of Middlemost (1994). (b) Zr/Ti versus Nb/Y of Winchester and Floyd (1976). (c-f) geochemical affinities plots including AFM diagram, SiO_2 versus K_2O relationship of Peccerillo and Taylor (1976), Co-Th diagram of Hastie et al. (2007) and Th/Yb versus Zr/Y diagram of Ross and Bédard (2009) showing that the El-Shadli bimodal suite belongs to the tholeiitic series and the intermediate rocks calc-alkaline series. Previously published data are from Abdel-Karim et al. (2019), Faisal et al. (2020), Khudeir et al. (1988), Shukri and Mansour (1980) and Stern et al. (1991).

Fig. 7: Chondrite-normalized REE patterns (Anders and Grevesse, 1989) and NMORB-normalized (Sun and McDonough, 1989) trace element diagram of the El-Shadli bimodal suite and intermediate rocks. MORB pattern is after Sun and McDonough (1989). Data for arc-basalts and granitoids are from GeoRoc (http://georoc.mpch-mainz.gwdg.de/georoc/). The previously published data are from (Faisal et al., 2020; Stern et al., 1991).

Fig. 8: Sr-Nd isotopic composition of rocks from the El-Shadli bimodal volcanic province. MORB and OIB fields are after Hofmann (2014). The ANS N-MORB ophiolite data are those from W. Gerf to the south of the study area (Zimmer et al., 1995) and W. Ghadir to the north of the study area (Basta et al., 2011).

Fig. 9: SHRIMP and LA-SS-ICPMS geochronological data and CL images of samples from the El-Shadli volcanic province. (a, c) Zircon U-Pb SHRIMP Concordia diagrams showing the $^{206}Pb/^{238}U$ ages of the analysed zircons with 2 sigma errors. Weighted means, relative probability diagrams of $^{206}Pb/^{238}U$ ages, and representative CL images are shown for each sample. The red circles on the CL images mark the place for SHRIMP, LASS, and SIMS spot analyses for the U-Pb age, Hf and O isotopes, and trace element data, respectively. (b, d) Zircon U-Pb LASS Concordia diagrams showing the $^{206}Pb/^{238}U$ ages of the analysed zircons with 2 sigma errors. Weighted means and relative probability diagrams of $^{206}Pb/^{238}U$ age are shown for each sample.

Fig. 10: Zircon Chondrite-normalized REE patterns (Anders and Grevesse, 1989) and trace element composition tectono-magmatic classification of the El-Shadli volcanic province using the classification fields of Grimes et al. (2007, 2015).

Fig. 11: Age, Hf, and O isotopic data of zircon from the El-Shadli volcanic province. (a) εHf(t) vs $^{206}Pb/^{238}U$ age plot against the Chondritic uniform reservoir (CHUR) and depleted mantle (DM; Griffin et al., 2002) lines. Hf isotopic data of ANS magmatism (e.g., Morag et al., 2011, 2012; Robinson et al., 2014) are used for comparison. (b) The plot of $\delta^{18}O$ vs εHf(t) for the studied zircons. Old upper and lower crust trends are from Kemp et al. (2007) and Wang et al. (2016). The typical mantle zircon (5.3 ± 0.3‰) is from Valley et al. (1998, 2005).

Fig. 12: Density and histogram of silica contents in rocks from the El-Shadli bimodal volcanic province compared the silica content in other Eastern Desert volcanics and well-studied arc- and rift-related volcanics. (a) The El-Shadli bimodal volcanic province data include that of this study, and previous work (Abdel-Karim et al., 2019; Faisal et al., 2020; Khudeir et al., 1988; Shukri and Mansour, 1980; Stern et al., 1991). (b-d) Data of other Eastern Desert volcanics including ophiolite-related volcanics (Abd El-Rahman et al., 2009b, 2009a; Basta et al., 2011; El-Sayed et al., 1999; Stern, 1981), arc-related volcanics (Ali et al., 2009) and the Dokhan volcanics (Eliwa et al., 2006, 2014) (Figure 4.14a-d). (e) Global database (after GeoRoc: http://georoc.mpch-mainz.gwdg.de/georoc/) of oceanic arc (IBM) and continental arc (Andean arc) volcanics and rift-related volcanics (the East-African rift).

Fig. 13: Tectonic discrimination diagrams for rocks from the El-Shadli bimodal volcanic province. (a) V versus Ti (Shervais, 1982; X.-C. Wang et al., 2016); (b) ternary Sm-Ti-V (Vermeesch, 2006); (c) TiO_2/Yb versus Nb/Yb (Pearce, 2008). The mafic rocks from the El-Shadli volcanic province plot in the MORB field similar to that of the Basin-and-Range rift-related basalts (X.-C. Wang et al., 2016), and intermediate rocks plot in the arc-related volcanics field. (d) SiO_2 versus FeO_T/(FeO_T + MgO) ratio (Frost et al., 2001), where the felsic rocks show similarity to A-type granites. (e, f) Rb vs. Y + Nb and Nb vs. Y of Pearce (1996), Pearce et al. (1984) and Whalen and Hildebrand (2019); the El Shadli felsic rocks are similar to ocean ridge granites (ORG) and show a slight overlap with within-plate granites (WPG), thus supporting a rift-related origin.

Fig. 14: Whole-rock petrogenetic discrimination diagrams. (a) εNd(t) vs. MgO (wt. %) after Li et al. (2005) and (b) La/Yb vs. La showing that the El-Shadli bimodal volcanic suite represents a coherent magmatic series fractionated from MORB-Like melts. (d) La vs. SiO_2 (wt. %) diagram modified after Brophy (2009) that suggests a partial melting origin.

Fig. 15: A proposed tectonic model for the genesis of the El-Shadli bimodal volcanic province. (a) Oceanic spreading and ridge magmatism, and possible subduction at a continental arc during ~830–750 Ma with hydrothermal fluids circulating and altering the lower crust section of the oceanic crust near MOR. (b) Accretion of oceanic slabs along the subduction zone during ~750–730 Ma, forming a juvenile accreted terrane. (c) Rifting and formation of the bimodal volcanic province by partial melting the lower crust of the accreted oceanic slabs driven by a mantle plume at ~ 700 Ma.

Figure.1

Click here to access/download;Figure;Fig. 1.jpg

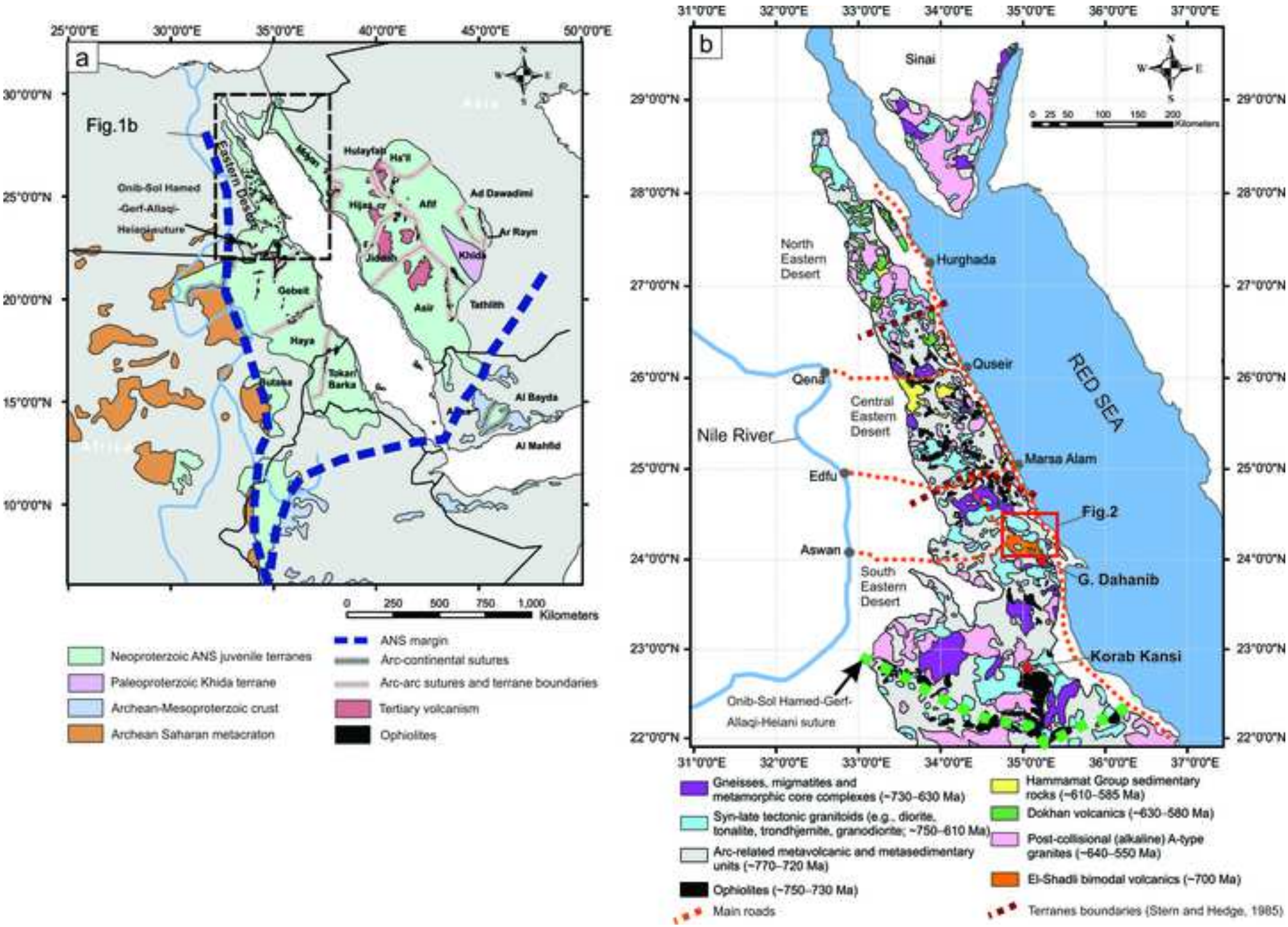

Figure.2

Click here to access/download;Figure;Fig. 2.jpg

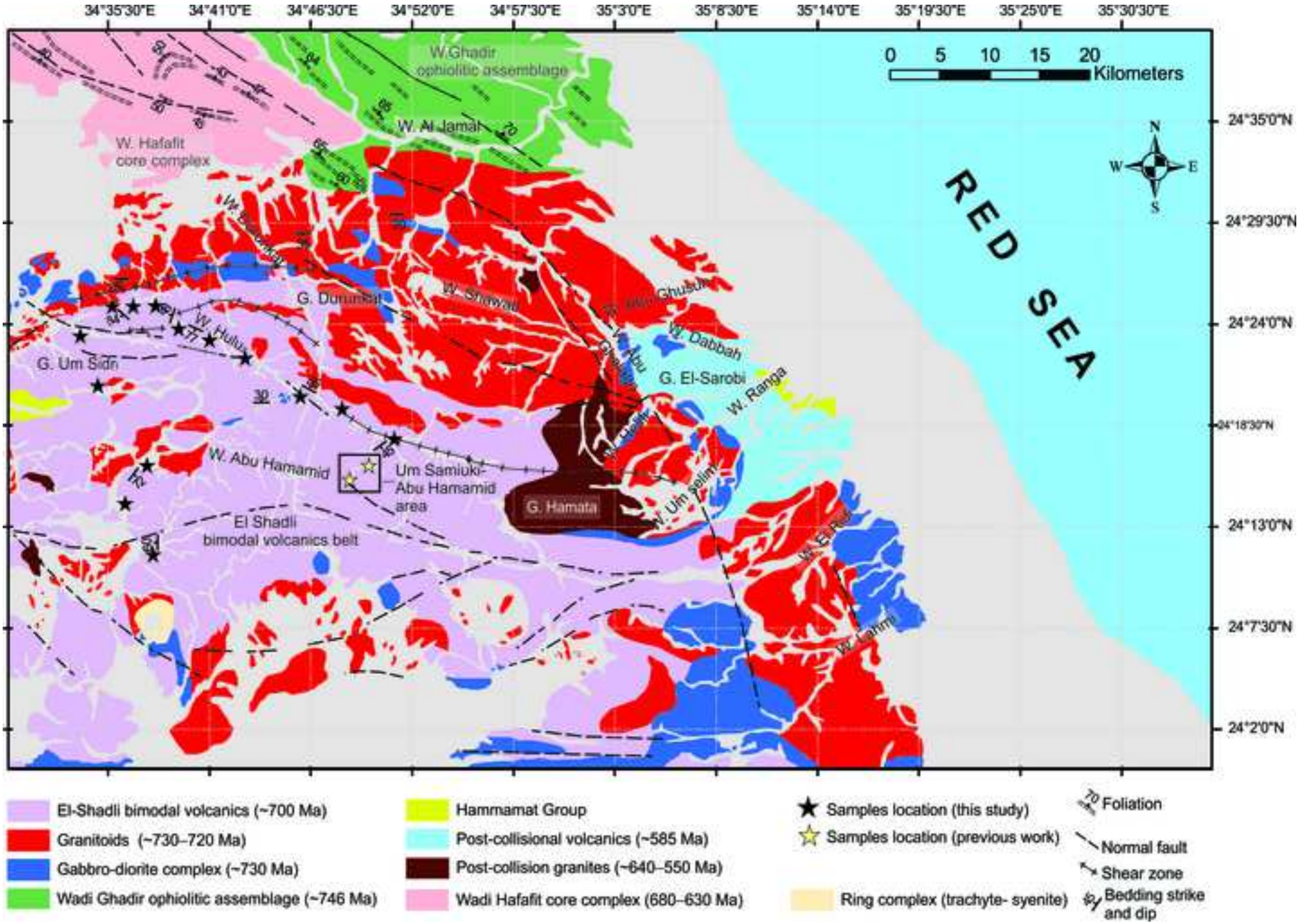

Figure.3

Click here to access/download;Figure;Fig. 3.jpg

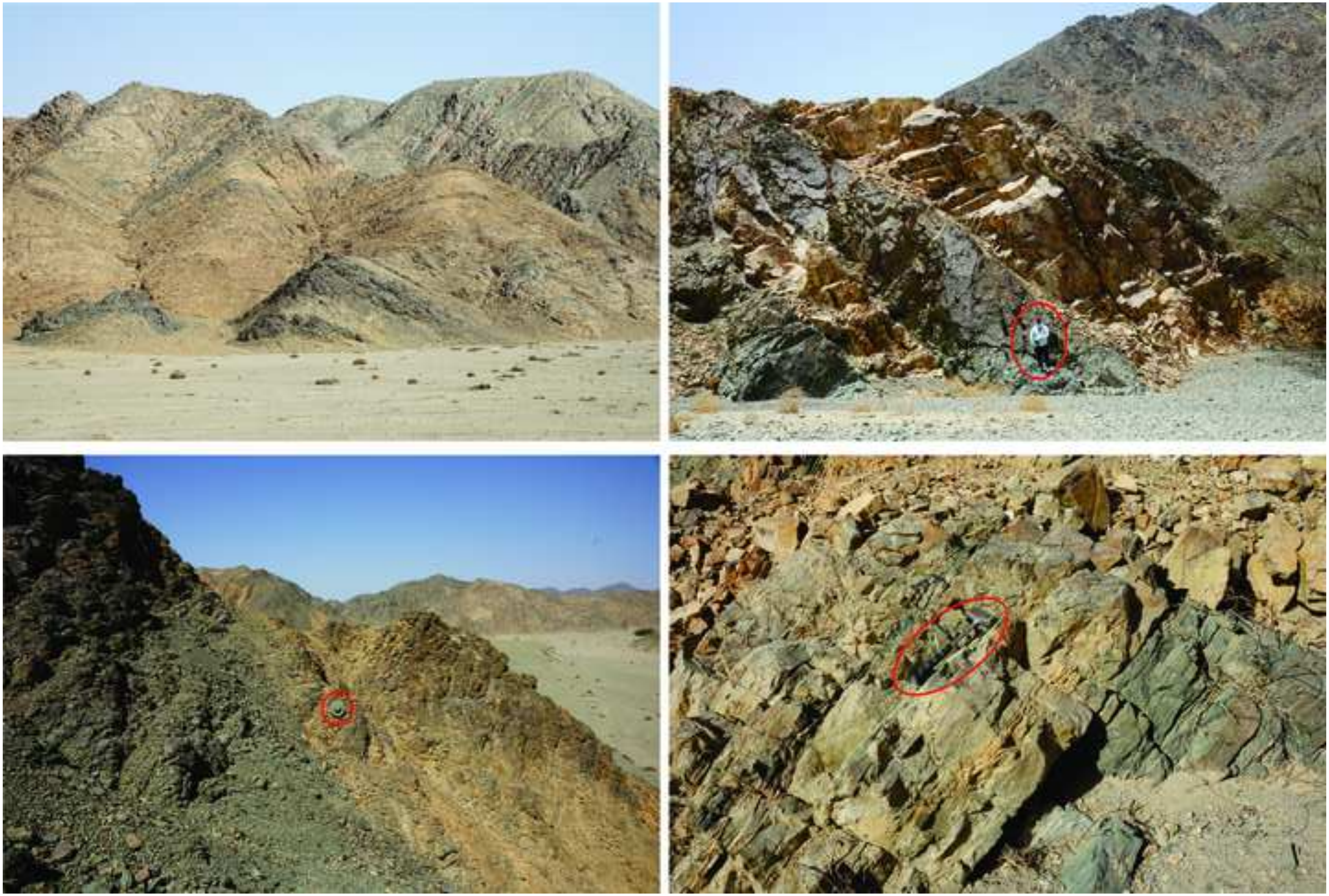

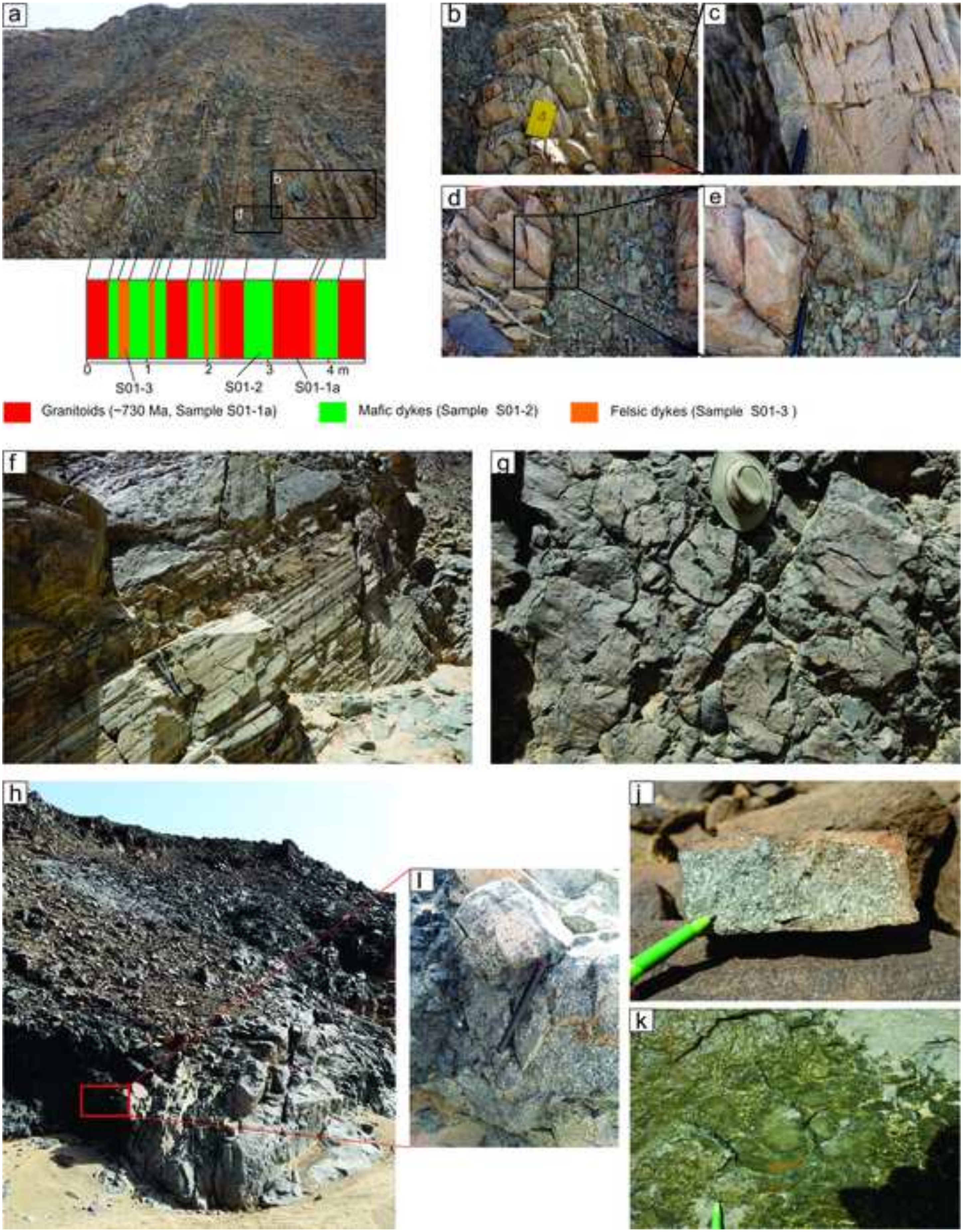
a
b
c
d
e
b
d
0
1
2
3
4 m
S01-3
S01-2
S01-1a
Granitoids (~730 Ma, Sample S01-1a)
Mafic dykes (Sample S01-2)
Felsic dykes (Sample S01-3)
f
g
h
i
j
k

Figure.5

Click here to access/download;Figure;Fig. 5.jpg

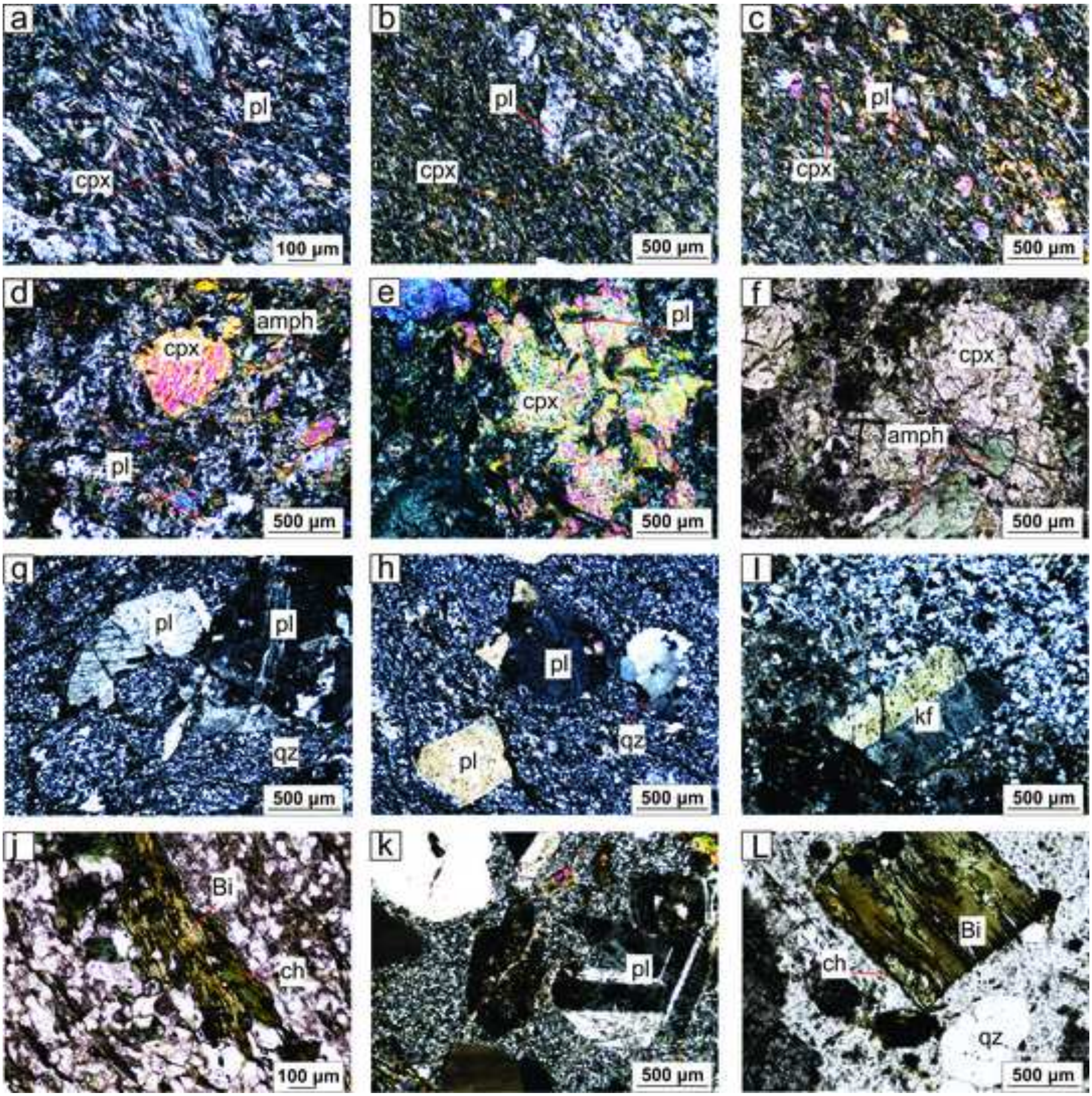

Figure.6

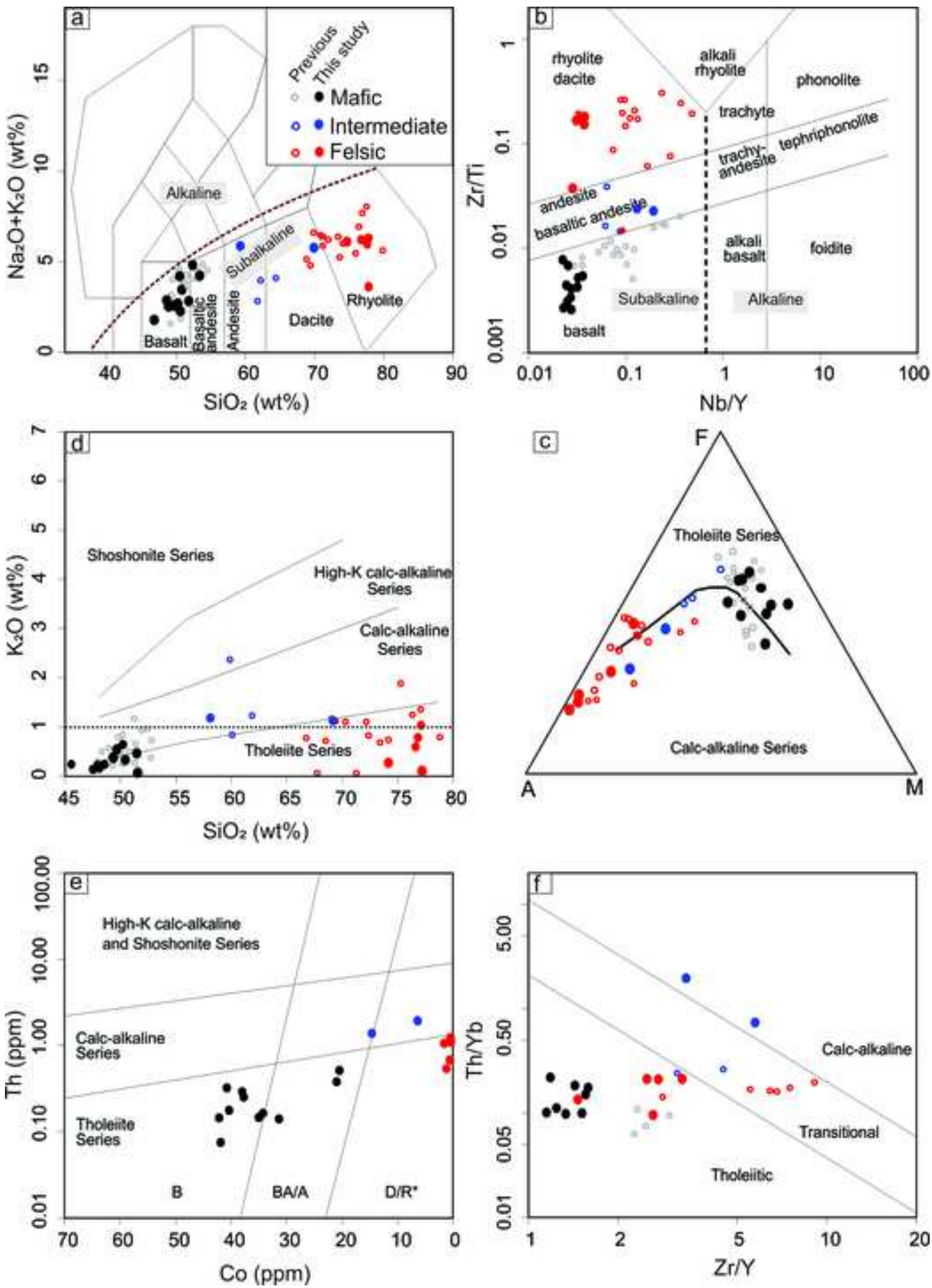

a
Previous
This study
Mafic
Intermediate
Felsic
Alkaline
Subalkaline
Basalt
Basaltic andesite
Andesite
Dacite
Rhyolite
Na2O+K2O (wt%)
SiO2 (wt%)
b
rhyolite dacite
alkali rhyolite
phonolite
trachyte
trachy-andesite
tephriphonolite
andesite
basaltic andesite
alkali basalt
foidite
Subalkaline
Alkaline
basalt
Zr/Ti
Nb/Y
d
Shoshonite Series
High-K calc-alkaline Series
Calc-alkaline Series
Tholeiite Series
K2O (wt%)
SiO2 (wt%)
c
F
Tholeiite Series
Calc-alkaline Series
A
M
e
High-K calc-alkaline and Shoshonite Series
Calc-alkaline Series
Tholeiite Series
B
BA/A
D/R*
Th (ppm)
Co (ppm)
f
Calc-alkaline
Transitional
Tholeiitic
Th/Yb
Zr/Y

Figure.7

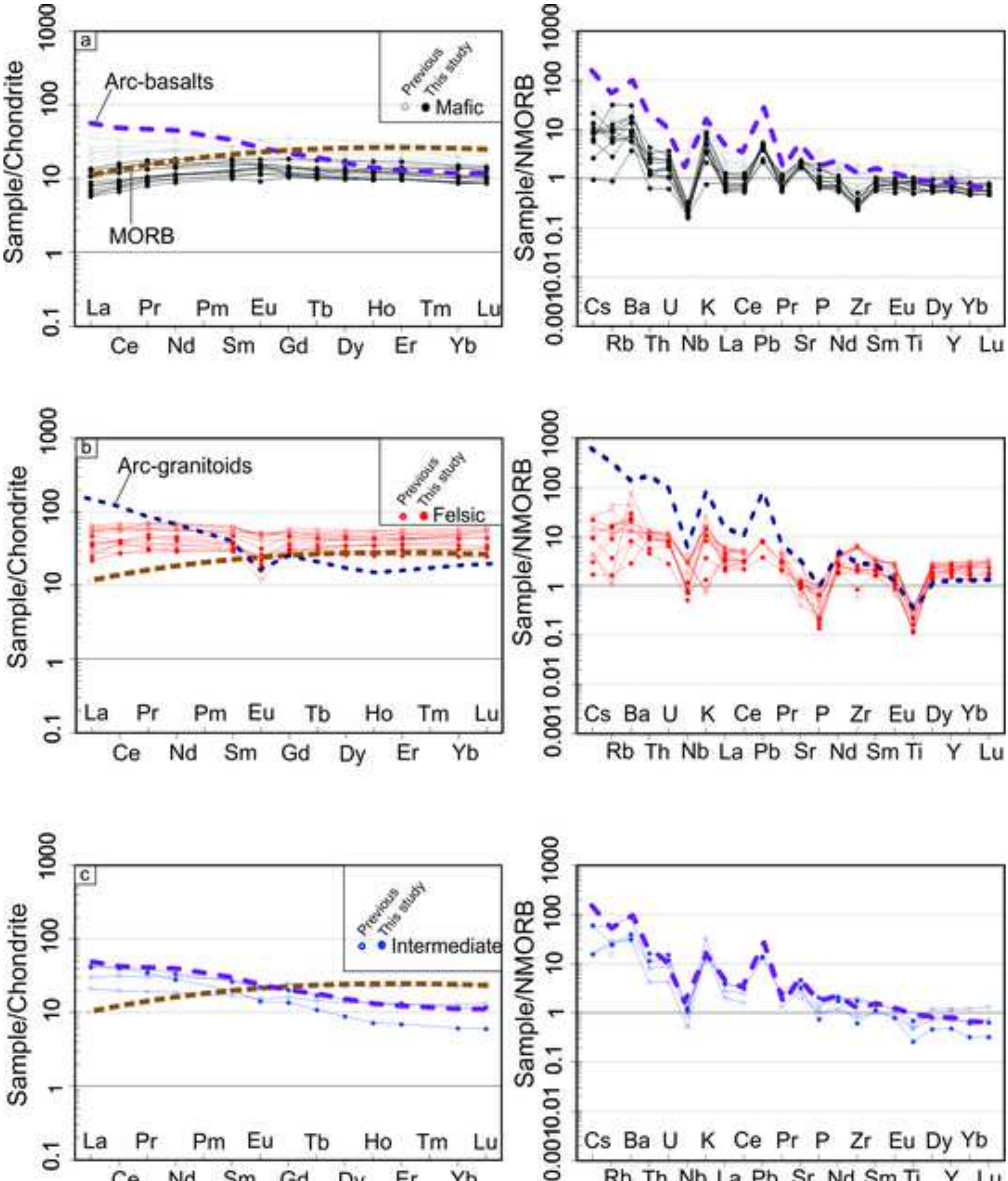
a
Arc-basalts
MORB
Previous
This study
Mafic
Sample/Chondrite
Sample/NMORB
b
Arc-granitoids
Previous
This study
Felsic
c
Previous
This study
Intermediate
0.1
1
10
100
1000
0.001
0.01
La Pr Pm Eu Tb Ho Tm Lu
Ce Nd Sm Gd Dy Er Yb
Cs Ba U K Ce Pr P Zr Eu Dy Yb
Rb Th Nb La Pb Sr Nd Sm Ti Y Lu

Figure.8

Click here to access/download;Figure;Fig. 8.jpg

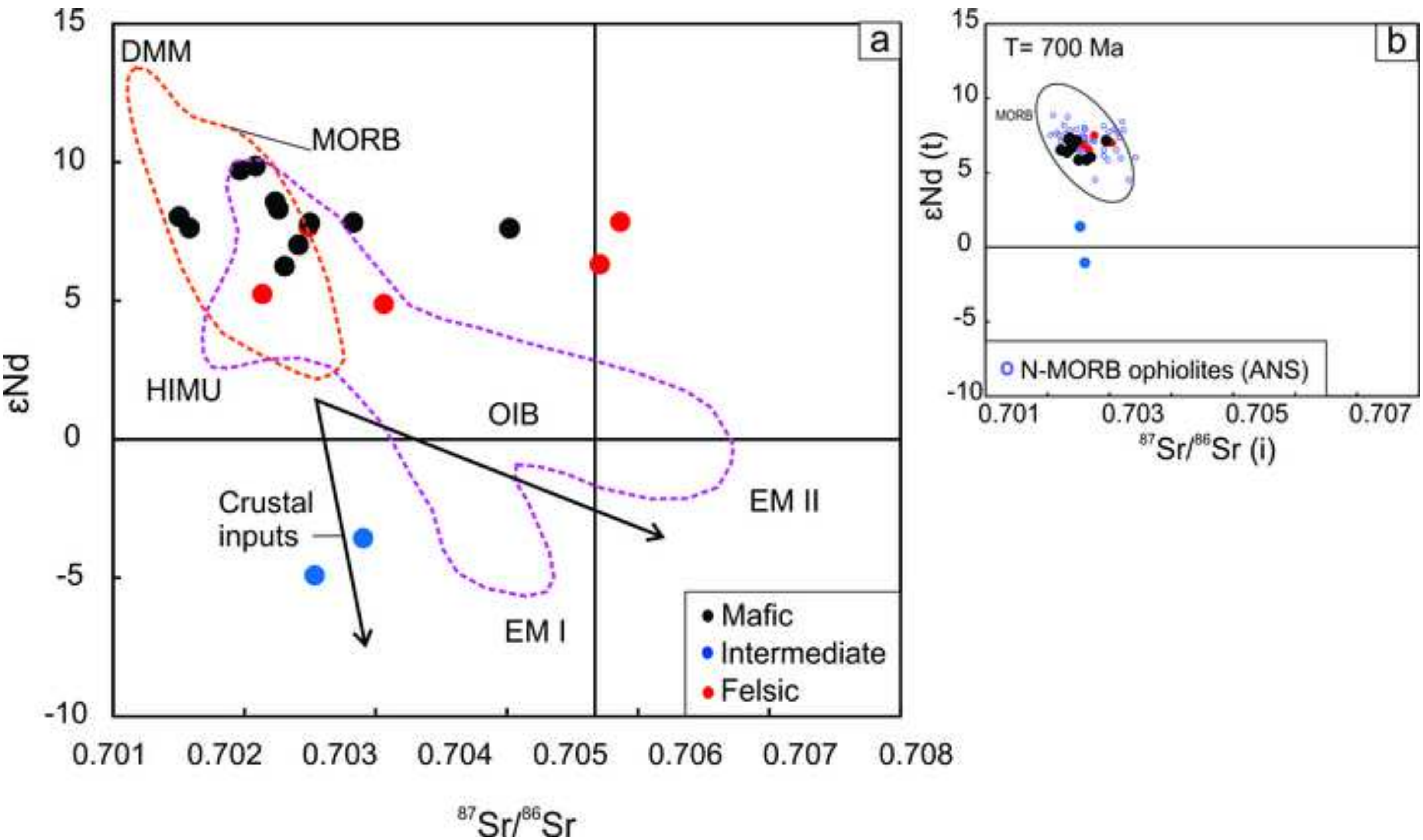

Figure.9

Click here to access/download;Figure;Fig. 9.jpg

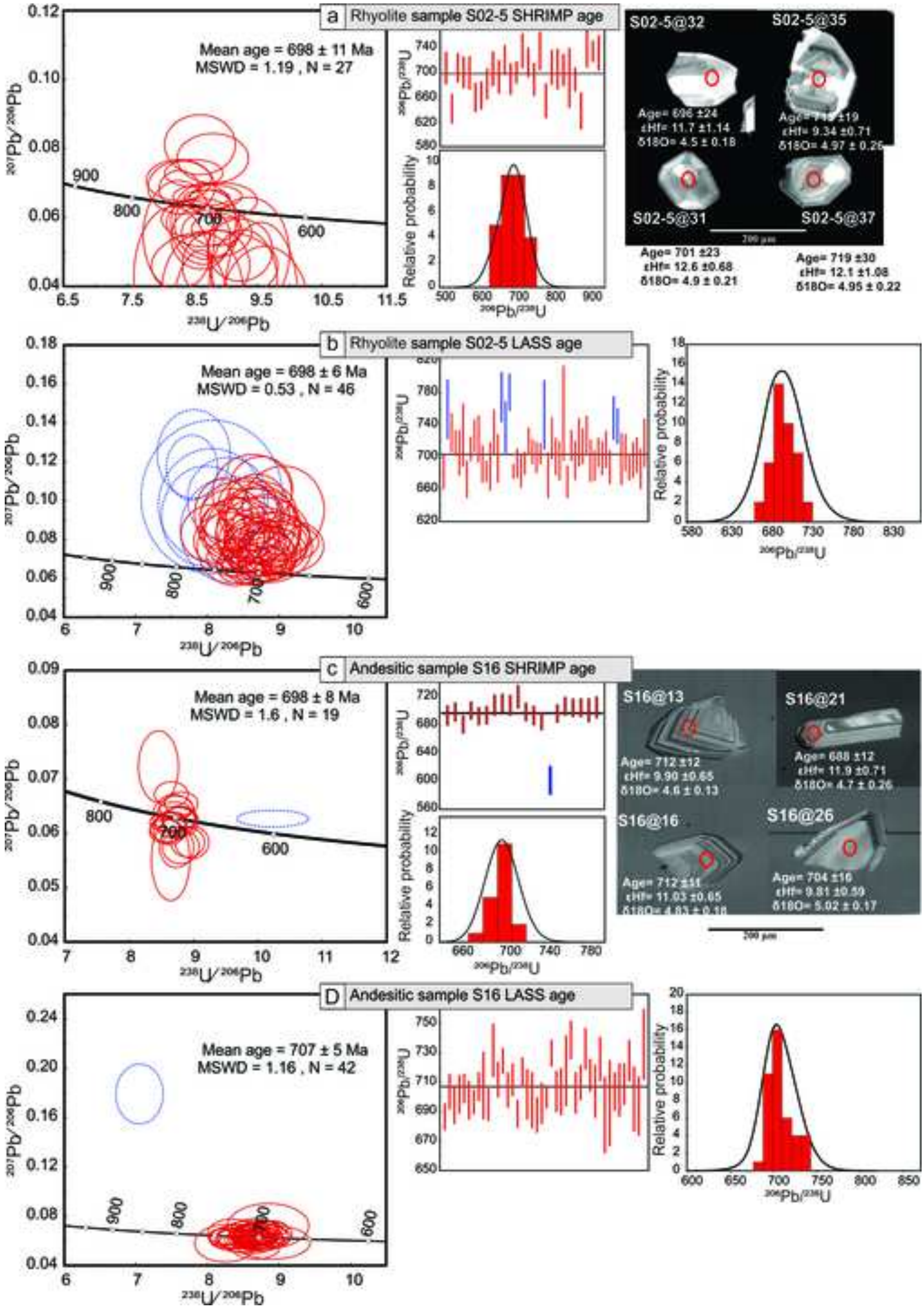

Figure.10

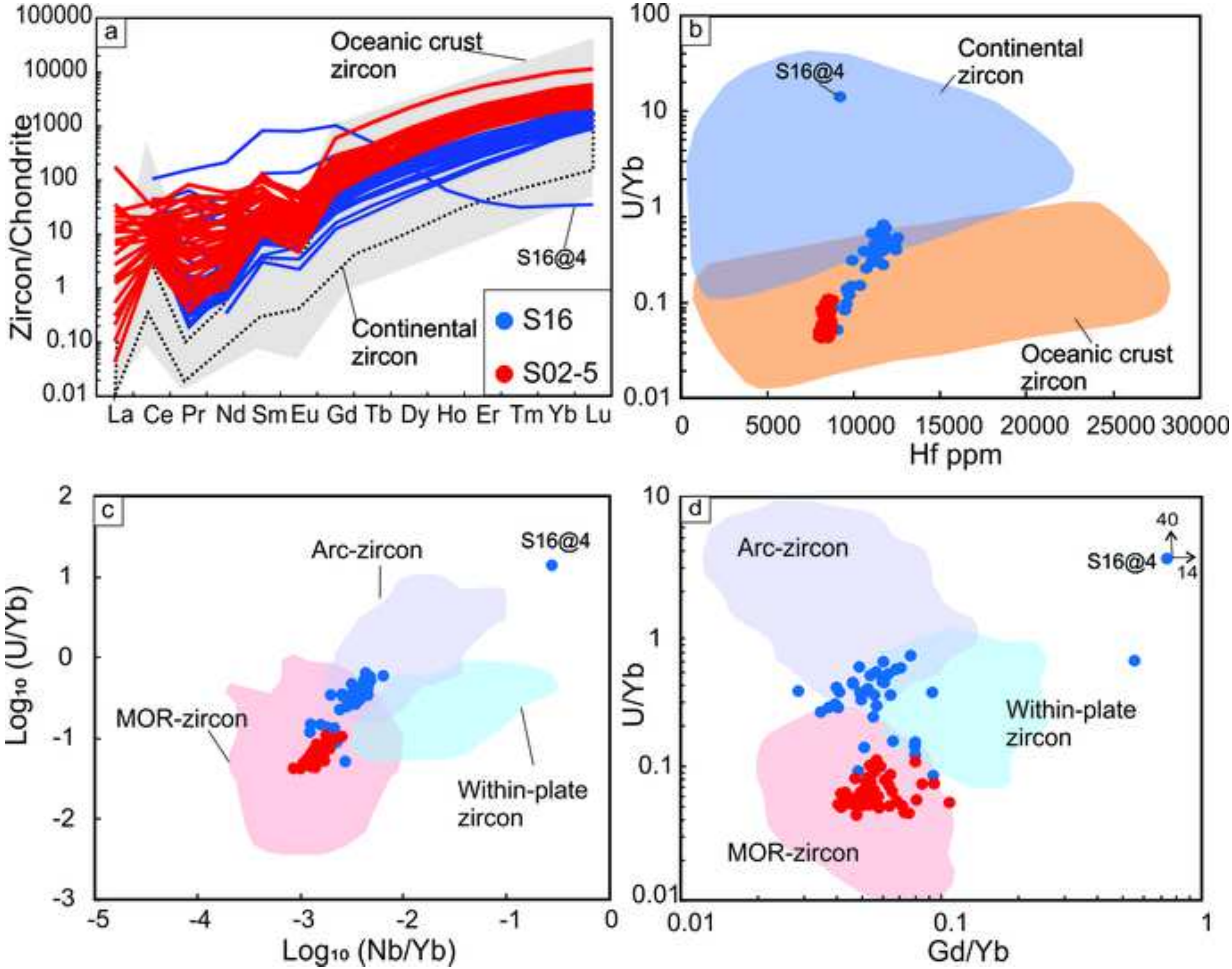
a
Oceanic crust zircon
Continental zircon
S16@4
S16
S02-5
Zircon/Chondrite
100000
10000
1000
100
10
1
0.10
0.01
La Ce Pr Nd Sm Eu Gd Tb Dy Ho Er Tm Yb Lu
b
Continental zircon
Oceanic crust zircon
S16@4
U/Yb
100
10
1
0.1
0.01
0 5000 10000 15000 20000 25000 30000
Hf ppm
c
Arc-zircon
MOR-zircon
Within-plate zircon
S16@4
Log10 (U/Yb)
2
1
0
-1
-2
-3
-5 -4 -3 -2 -1 0
Log10 (Nb/Yb)
d
Arc-zircon
Within-plate zircon
MOR-zircon
S16@4
40
14
U/Yb
10
1
0.1
0.01
0.01 0.1 1
Gd/Yb

Figure.11

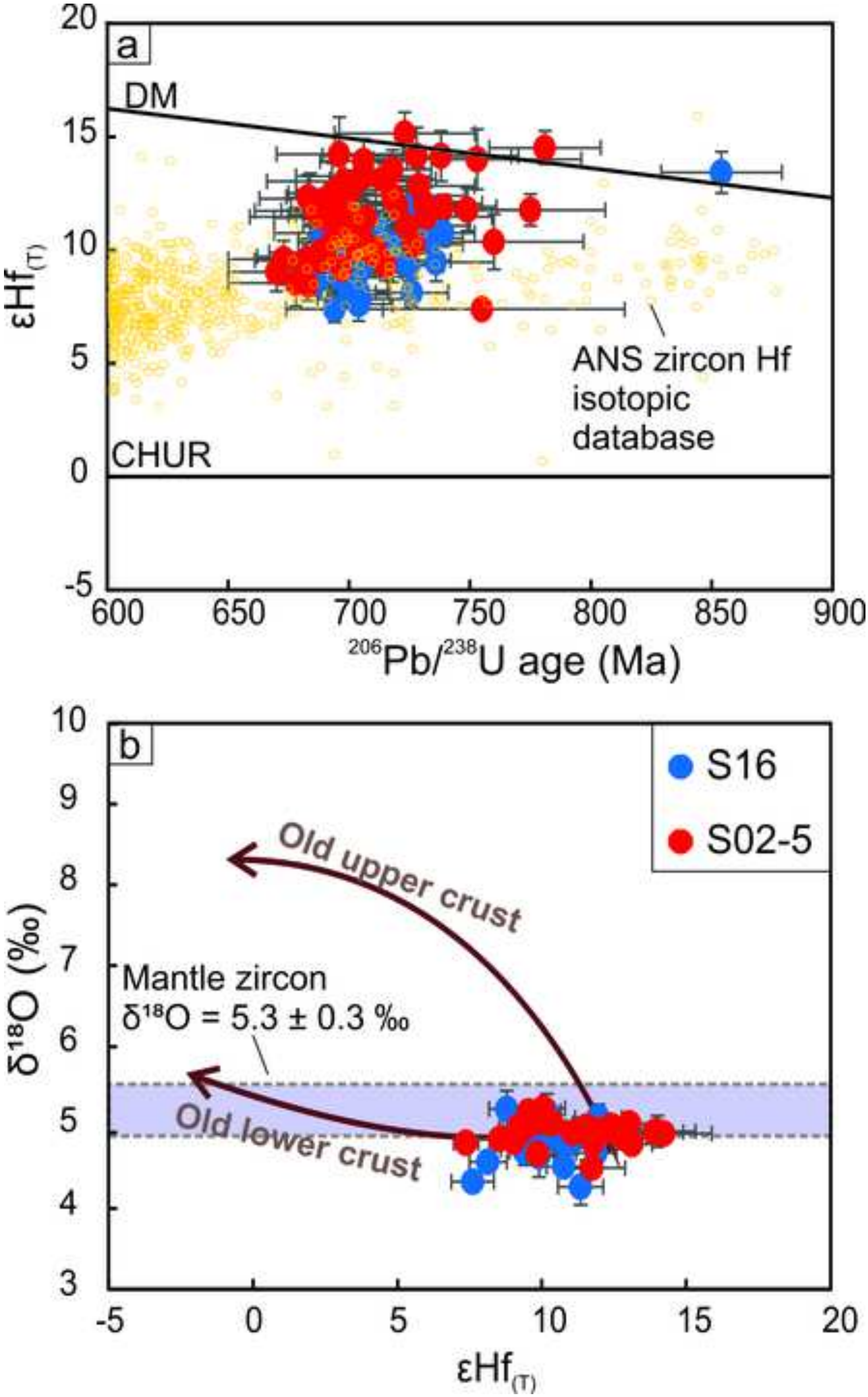
a
DM
CHUR
ANS zircon Hf
isotopic
database
εHf(T)
206Pb/238U age (Ma)
b
S16
S02-5
Old upper crust
Old lower crust
Mantle zircon
δ18O = 5.3 ± 0.3 ‰
δ18O (‰)
εHf(T)

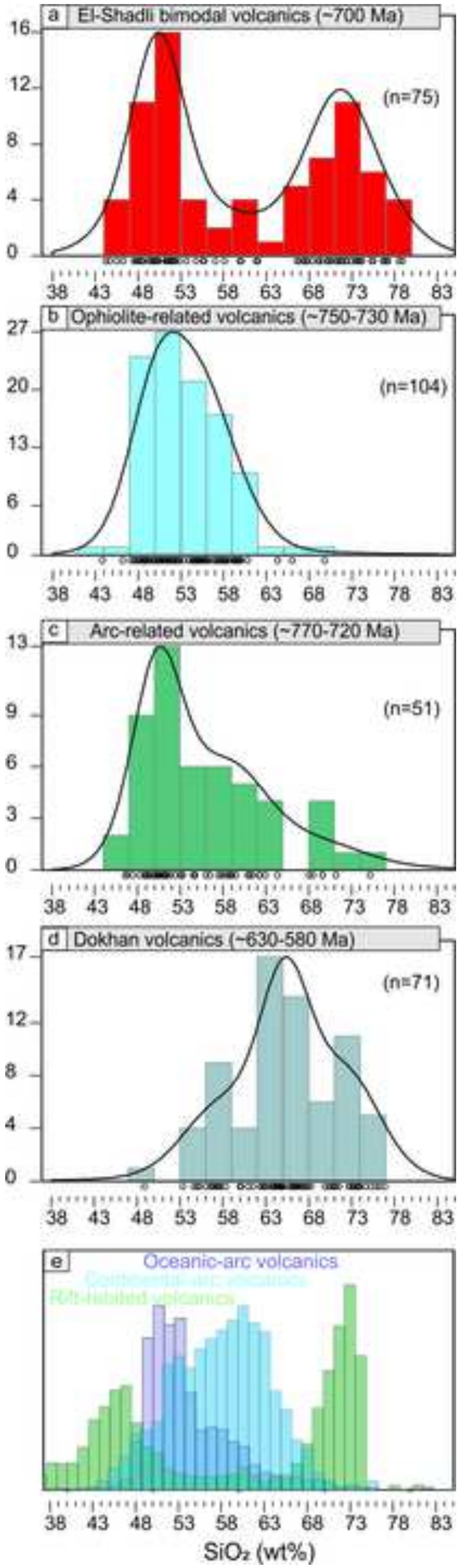
a El-Shadli bimodal volcanics (~700 Ma)
(n=75)
b Ophiolite-related volcanics (~750-730 Ma)
(n=104)
c Arc-related volcanics (~770-720 Ma)
(n=51)
d Dokhan volcanics (~630-580 Ma)
(n=71)
e
Oceanic-arc volcanics
Continental-arc volcanics
Rift-related volcanics
38 43 48 53 58 63 68 73 78 83
SiO₂ (wt%)

Figure.13

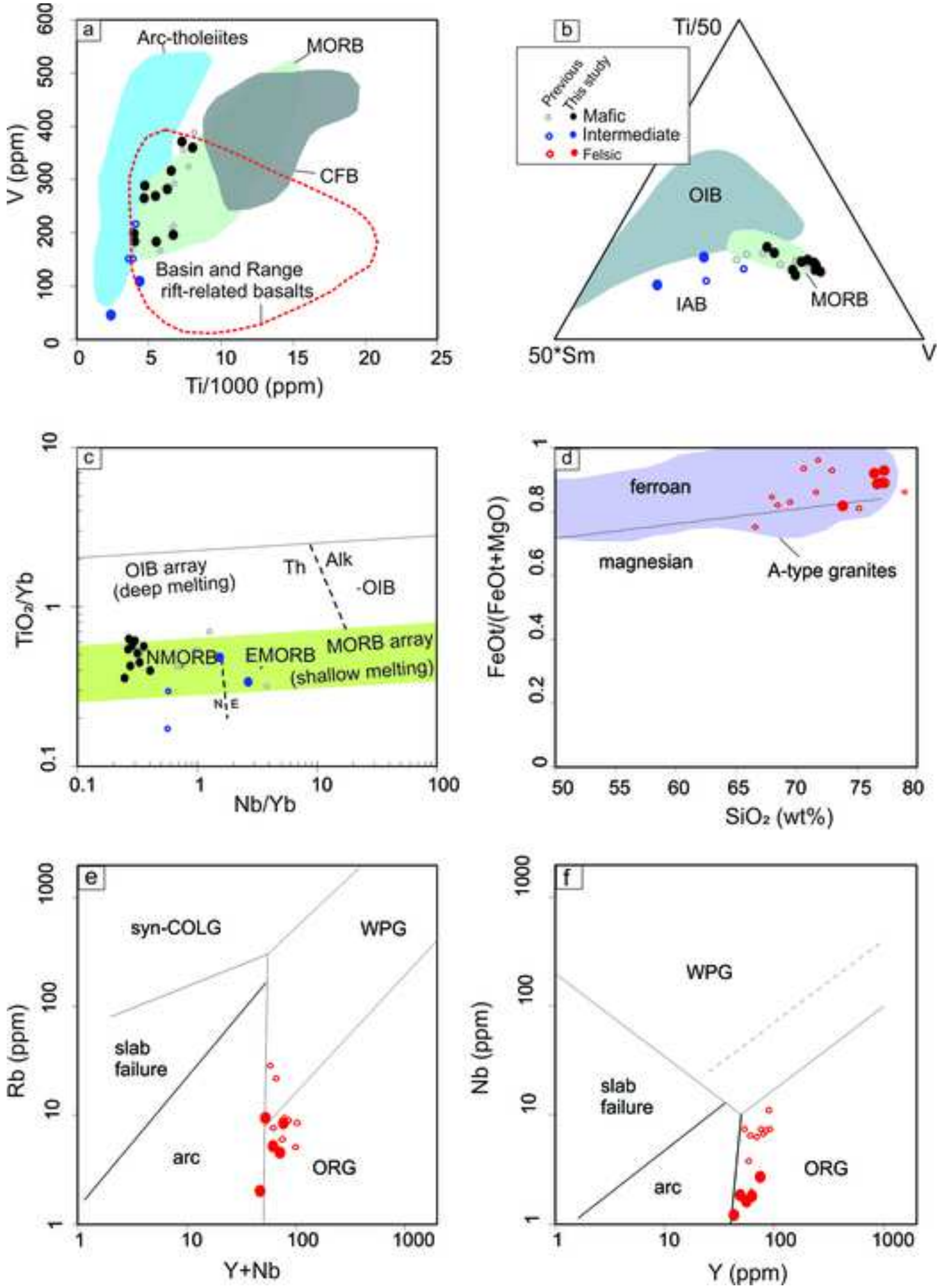
a
Arc-tholeiites
MORB
CFB
Basin and Range
rift-related basalts
V (ppm)
Ti/1000 (ppm)
b
Ti/50
Previous
This study
Mafic
Intermediate
Felsic
OIB
IAB
MORB
50*Sm
V
c
OIB array
(deep melting)
Th
Alk
-OIB
NMORB
EMORB
MORB array
(shallow melting)
N E
TiO₂/Yb
Nb/Yb
d
ferroan
magnesian
A-type granites
FeOt/(FeOt+MgO)
SiO₂ (wt%)
e
syn-COLG
WPG
slab
failure
arc
ORG
Rb (ppm)
Y+Nb
f
WPG
slab
failure
arc
ORG
Nb (ppm)
Y (ppm)

Figure.14

Click here to access/download;Figure;Fig. 14.jpg

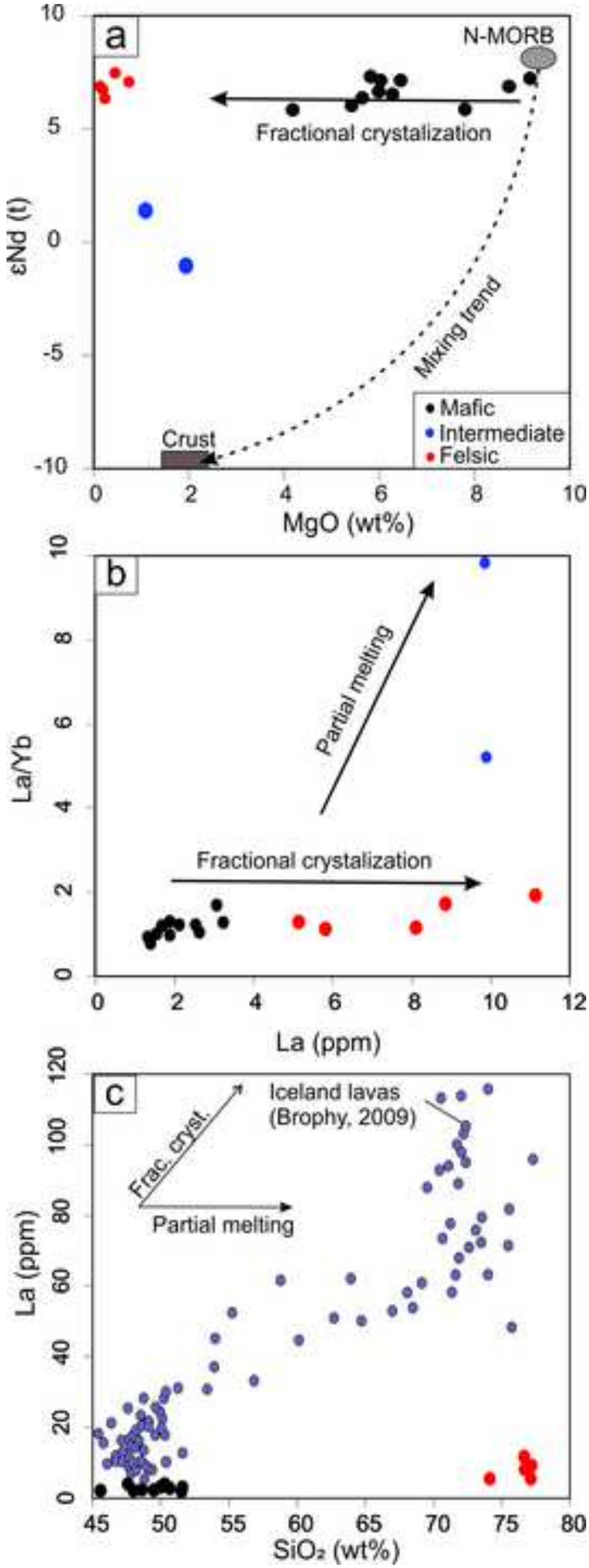

Figure.15

Click here to access/download;Figure;Fig. 15.jpg

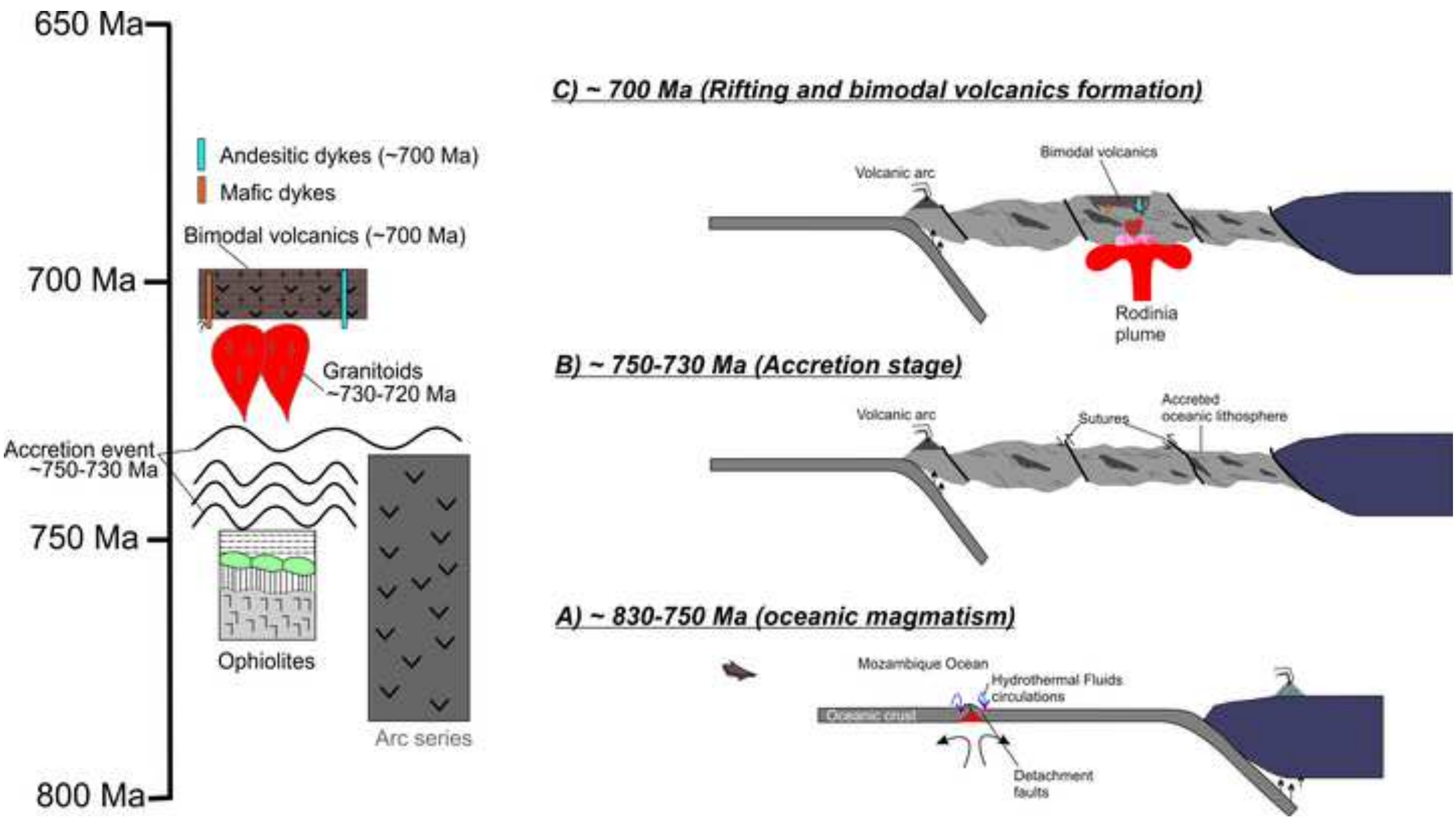

Declaration of Competing Interest

The authors declare that they have no known competing financial interests or personal relationships that could have appeared to influence the work reported in this paper

CRediT authorship contribution statement

HG: Conceptualization, Formal analysis, Investigation, Methodology, Writing - original draft. **ZXL:** Conceptualization, Formal analysis, Funding acquisition, Investigation, Methodology, Writing - review and editing, **MA:** Project administration, Investigation, Writing - review and editing. **LSD**: Formal analysis, Investigation, Methodology, Writing - review and editing. **JBM**: Conceptualization, Writing - review and editing. **NJE**: Formal analysis, Methodology, Writing - review and editing. **XPX**: Formal analysis, Methodology, Writing - review and editing. **JL**: Formal analysis, Methodology, Writing - review and editing